Biochemical and Biophysical Research Communications 388 (2009) 589–594

Contents lists available at ScienceDirect

Biochemical and Biophysical Research Communications

journal homepage: www.elsevier.com/locate/ybbrc

Ferritin reporter used for gene expression imaging by magnetic resonance

Kenji Ono, Kazuya Fuma, Kaori Tabata, Makoto Sawada *

Department of Brain Functions, Division of Stress Adaptation and Protection, Research Institute of Environmental Medicine, Nagoya University, Nagoya, Aichi 464-8601, Japan

ARTICLE INFO

Article history:
Received 3 August 2009
Available online 14 August 2009

Keywords:
Magnetic resonance imaging
Optical imaging
Gene expression
Glioma

ABSTRACT

Magnetic resonance imaging (MRI) is a minimally invasive way to provide high spatial resolution tomograms. However, MRI has been considered to be useless for gene expression imaging compared to optical imaging. In this study, we used a ferritin reporter, binding with biogenic iron, to make it a powerful tool for gene expression imaging in MRI studies. GL261 mouse glioma cells were over-expressed with dual-reporter ferritin–DsRed under β-actin promoter, then gene expression was observed by optical imaging and MRI in a brain tumor model. GL261 cells expressing ferritin–DsRed fusion protein showed enhanced visualizing effect by reducing T2-weighted signal intensity for *in vitro* and *in vivo* MRI studies, as well as DsRed fluorescence for optical imaging. Furthermore, a higher contrast was achieved on T2-weighted images when permeating the plasma membrane of ferritin–DsRed-expressing GL261. Thus, a ferritin expression vector can be used as an MRI reporter to monitor *in vivo* gene expression.

Introduction

Magnetic resonance imaging (MRI) is one of the minimally invasive imaging techniques for high spatial resolution tomograms providing anatomical and functional information. Other tomographic imaging techniques like computed tomography (CT) and positron emission tomography (PET) generally entails radiation exposure, unlike MRI, which is free from radiation exposure. Therefore, MRI is accepted as a safer imaging technique compared to others, though it is unsuitable for visualization of gene expression. As a result, optical imaging is generally used for this purpose because several fluorescent and chemiluminescent reporters such as GFP and DsRed and luciferase enzyme systems are available [1]. The availability of gene products capable of altering local signals of MRI for contrast, will be a useful MRI reporter for gene expression.

Iron derivatives are common MRI contrast agents that decrease signal intensity on T2-weighted images as a result of the magnetic susceptibility effect [2]. Thus, localized accumulation of iron derivates are detected by MRI [3]. In fact, iron derivates such as ferumoxides and ferric ammonium citrate are useful in clinical diagnosis of liver neoplasm [4] and gastrointestinal tract [5], respectively. Recent studies suggest use of genes encoding iron-binding proteins as a potential candidate of MRI reporter for *in vivo* MRI detection of gene expression [6].

Ferritin, an endogenous iron storage metalloprotein, consists of 24 light and heavy polypeptide chains encapsulating an iron oxide core with up to 4500 iron atoms [7]. Heavy chain of ferritin mainly binds to iron oxide [8]. Ferritin further creates magnetic fields that affect relaxation time of water protons diffusing through the magnetic field [9]. This makes heavy chain of ferritin an ideal MRI reporter for *in vivo* gene expression in MRI studies.

In this study, we designed a vector capable of expressing heavy chain of ferritin and DsRed fusion protein (ferritin–DsRed) under a β-actin promoter, and made ferritin–DsRed-overexpressing GL261 cell mouse clonal glioma cells, to detect the cells by *in vivo* and *in vitro* magnetic resonance imaging. Results of this study suggest that this ferritin reporter system was useful to detect *in vivo* gene expression by MRI.

Materials and methods

Cell lines. Murine GL261 glioma cells including DsRed expressing and ferritin–DsRed-expressing derivatives were cultured in Dulbecco's Modified Eagle's Medium (DMEM) (Sigma–Aldrich, St. Louis, MO, USA) with 10% fetal bovine serum and Penicillin–Streptomycin (Invitrogen, Carlsbad, CA, USA). Cells were regularly photographed under a fluorescent microscope (IX-70, Olympus, Tokyo, Japan).

Plasmids and electroporation. pferritin–DsRed plasmids were made from a pDsRed-N1 vector (CLONTECH Laboratories, Inc., Mountain View, CA, USA) by insertion of a mouse heavy chain of ferritin sequence (NM_010239). The mouse heavy chain of ferritin sequence was amplified by polymerase chain reaction, then PCR products were treated with restriction enzymes, HindIII and BamHI, and ligated into the pDsRed-N1 vector at the multi-cloning site. GL261 cells (1×10^6 cells/400 μl) were mixed with 10 μg of the

* Corresponding author. Fax: +81 52 789 3994.
E-mail address: msawada@riem.nagoya-u.ac.jp (M. Sawada).

0006-291X/$ - see front matter © 2009 Elsevier Inc. All rights reserved.
doi:10.1016/j.bbrc.2009.08.055

plasmids in a 4 mm gap cuvette. The cuvette was set in an ECM830 electroporator (BTX Instrument Division Harvard Apparatus, Inc., Holliston, MA, USA) and electroporation was performed under the following condition (Choose mode: LV mode, Set Voltage: 170 V, Set Pulse Length: 70 ms, Set Number of Pulses: 1). Electroporated cells were cultured in the medium with 400 μg/ml of G418 for selection of mixed clone expressed ferritin–DsRed for 7 days.

RNA extraction and RT-PCR. Total RNA was extracted from cells using RNeasy Mini kit and RNase-free DNase set (QIAGEN, Hilden, Germany) according to the manufacturer's instruction. RNA (1 μg) was reverse transcribed at 37 °C for 90 min in a mixture containing 100 U of recombinant M-MLV reverse transcriptase, 0.1 μg DNA random hexamers, 40 U RNase inhibitor and 1.4 mM dNTPs, in a final volume of 50 μl. The cDNA was amplified with *Taq* DNA polymerase (Takara, Tokyo, Japan), using primer pairs specific to DsRed (sense primer: TTC CAG TAC GGC TCC AAG GT; antisense primer: GAG GAG TCC TGG GTC ACG GT) and ferritin–DsRed (sense primer: CGA GAT GAT GTG GCT CTG AA; antisense primer: GAG GAG TCC TGG GTC ACG GT) for 35 cycles (94 °C for 1 min, 55 °C for 1 min, and 72 °C for 2 min) and glyceraldehyde 3 phosphate dehydrogenase, GAPDH (sense primer: TGC ACC ACC AAC TGC TTA G; antisense primer: GAT GCA GGG ATG ATG TTC) for 30 cycles, respectively. The PCR products were resolved by electrophoresis on 2% agarose gels stained with ethidium bromide, then photographed using Light Capture (ATTO Corporation, Tokyo, Japan).

Western blotting. Electroporated G261 cells (1×10^6 cells) were lysed on ice in 100 μl TNE buffer (10 mM Tris–HCl, pH 7.5, 1% NP-40, 0.15 M NaCl, 1 mM EDTA, 10 μg/ml approtinin, 10 μg/ml leupeptin), and sonicated before BCA protein quantification (Pierce, Rockford, IL, USA). Samples of equal protein quantity were separated on 12.5% SDS–PAGE gels and transferred to nitrocellulose membranes for Western blotting according to the iBlot gel transfer system (Invitrogen). To detect DsRed, we used anti-DsRed polyclonal rabbit antibody (CLONTECH Laboratories, Inc., 1:1000 dilution) and ECL plus detection system (GE Healthcare UK Ltd., Buckinghamshire, England). The same membrane was re-probed by anti-GAPDH monoclonal antibody and ECL plus detection took place after detection of DsRed.

FACS analysis. Fluorescence of DsRed in electroporated GL261 cells was analyzed using a FACSCalibur cell sorter (BD Bioscience, San Jose, CA, USA) equipped with a 530 nm filter (bandwidth ± 15 nm) and a 585 nm filter (bandwidth ± 21 nm) and CellQuest software (BD Bioscience).

Brain tumor model. Viable cells were counted using a hemocytometer, and the concentration was adjusted to 5×10^5 cells/5 μl of PBS. Each C57BL/6 mouse was anesthetized and placed in a stereotactic frame, then the skull was exposed. One millimeter of burr holes were drilled and the following coordinates were used to position the 10 μl Hamilton syringe, placing the needle 4.0 mm anterior to the bregma, 4.0 mm lateral to the midline, and 3.5 mm ventral to the cortical surface to deliver cells into the striatum. At each site, an injection volume of 5 μl was delivered at a rate of 1 μl/min, and the needle was withdrawn after an additional 5 min. At 3 weeks after injection, the hearts of anesthetized mice were perfused with about 100 ml isotonic saline, and then each brain was isolated, frozen in liquid nitrogen, and embedded in an OCT compound (Tissue Tek; Miles, Elkhart, IN, USA). In some cases, permeated cells by sonication for 1 min on ice were injected stereotactically into the brain, and the brain was similarly embedded after *in vivo* imaging.

Magnetic resonance imaging (MRI). Mice transplanted GL261 cells were anesthetized with 1.0% isoflurane and held in an MRI coil. It was set on MRI equipment (MRTechnology, Inc., Tsukuba, Japan) and T1 and T2-weighted images were acquired according to the manufacturer's procedure. Recombinant ferritin–DsRed from *Escherichia coli* or GL261 cells were collected in 1.5 ml tubes, and T1 and T2-weighted images were acquired by similar procedure.

Optical imaging. Anesthetized mice were observed using a Maestro (Cambridge Research & Instrumentation, Inc., MA, USA) *in vivo* imaging system equipped with LCTF (Liquid Crystal Tunable Filter), which was useful for spectral analysis between DsRed and autofluorescence. Coronal brain sections were also observed using Maestro, and DsRed-specific fluorescence was detected.

Immunohistochemical staining and Berlin blue staining. Coronal sections (8 μm) of the brains were cut with a cryostatmicrotome, transferred to a MAS coated slide glass (Matsunami Glass Ind., Ltd., Osaka, Japan) and immediately air-dried. Following fixation with 4% paraformaldehyde in PBS (pH 7.2) at room temperature for 10 min, sections were incubated in a blocking buffer (1% bovine serum albumine, 10% normal goat serum, and 0.01% sodium azide) for 30 min at room temperature and labeled with polyclonal antibodies against DsRed at a dilution of 1:500 for 1 h at room temperature. Then sections were visualized with Cy2-conjugated goat anti-rabbit IgG (Rockland Immunochemicals, Inc., Gilbertsville, PA, USA) and counterstained with Hoechst 33342 (Invitrogen, Carlsbad, CA, USA). Several sections were stained with Berlin blue staining. In brief, sections were fixed with ethanol at room temperature for 10 min and washed three times with PBS. The sections were incubated in a mixture of 2% potassium ferrocyanide solution with 1% HCl in equal amounts for 20 min at room temperature and counterstained with Kernechtrot solution (Muto Pure Chemicals Co. Ltd., Tokyo, Japan). Photographs of these sections were then taken under a fluorescent microscope (BX-50, Olympus, Tokyo, Japan).

Image analysis. Images acquired from optical imaging and from MRI were analyzed using Maestro software (Cambridge Research & Instrumentation, Inc.) and Image-Pro Plus software (Roper Industries, Inc., Sarasota, FL, USA), respectively.

Results

Some GL261 cells expressed DsRed at 24 h after electroporation, and the transformants expressing ferritin–DsRed were concentrated by G418 selection (Fig. 1A). FACS analysis showed that ferritin–DsRed-expressing GL261 cells had lower fluorescence compared to DsRed only expressing cells (Fig. 1B). To confirm transgene expression, mRNA expression of DsRed and ferritin–DsRed was analyzed by RT-PCR (Fig. 1C). GL261 cells, electroporated with pferritin–DsRed vectors, were positive for mRNA of both heavy chain of ferritin and DsRed. In addition, analysis by Western blotting indicated existence of ferritin–DsRed fusion protein in lysates from GL261 cells electroporated with pferritin–DsRed vectors (Fig. 1D). To determine whether ferritin–DsRed fusion protein in GL261 cells served as an MRI reporter, the cell pellet (Fig. 2A) was analyzed by T1-weighted images and T2-weighted images (Fig. 2B), since T1-weighted images are generally useful in investigating anatomical structures and T2-weighted images are effective in finding lesion sites in tissues by increasing the signal intensity. T2-weighted images are also highly effective in visualizing existence of iron in high T2-weighted signal intensity in animal tissues. As the first step to examination, we examined recombinant ferritin–DsRed fusion protein from *E. coli* using MRI. In general, T2-weighted images from proteinous pellets (data not shown) or cell pellets (Fig. 2B; middle) in aqueous liquid showed high intensity, however, we found that T2-weighted images from recombinant ferritin–DsRed indicated enhanced visualizing effect by reduction of T2-weighted signal intensity; dense deposits were observed at a site of a pellet (Fig. 2B; top). As the following step, cell pellets from ferritin–DsRed-expressing GL261 cells were observed using

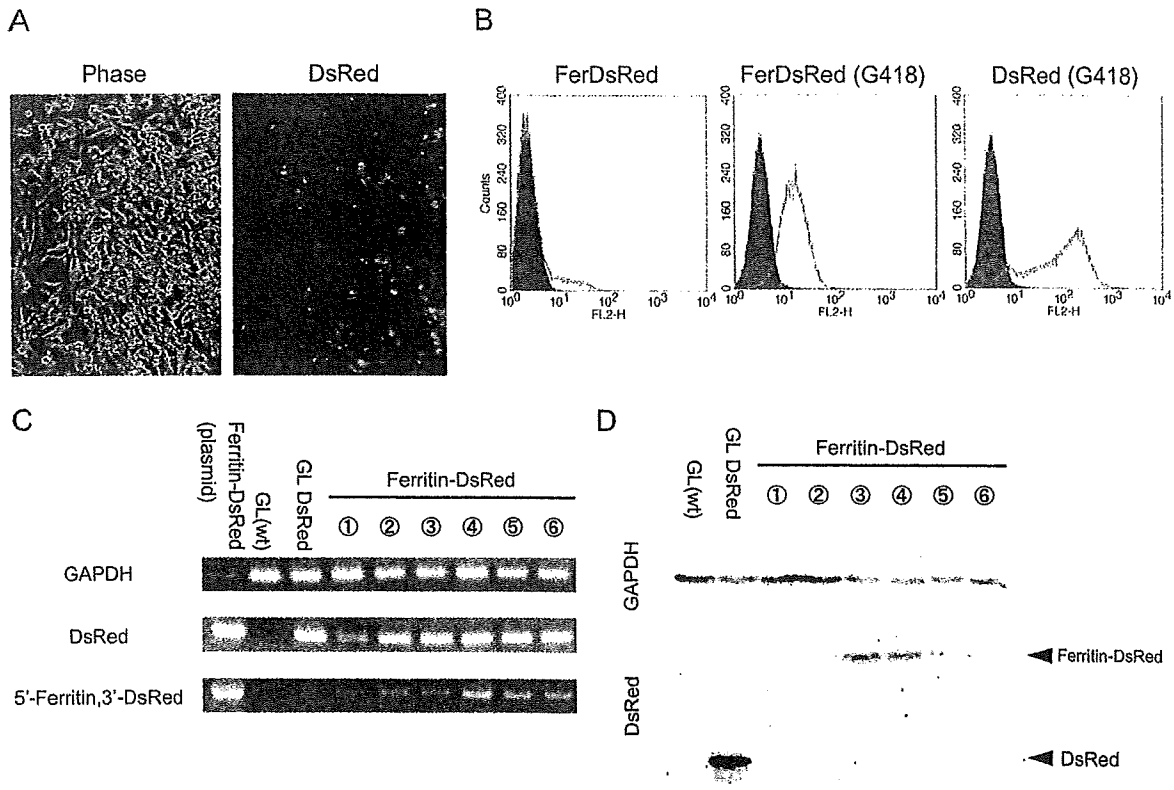

Fig. 1. Production of ferritin–DsRed-expressing GL261 cells. Photographs of ferritin–DsRed-expressing GL261 cells were taken after G418 selection (A). DsRed fluorescence intensity of electroporated GL261 cells was analyzed by FACS (B). The solid line in the left histogram indicated ferritin–DsRed-expressing GL261 cells before G418 selection, the solid line in the center histogram indicated ferritin–DsRed-expressing GL261 cells after G418 selection, and solid line in the right histogram indicated DsRed-expressing GL261 cells after G418 selection. A filled histogram in each histogram indicated GL261 cells. Gene transfer and expression for ferritin–DsRed was confirmed by RT-PCR (C) and Western blotting (D). Ferritin–DsRed (protein); recombinant ferritin–DsRed fusion protein from *E. coli*, GL (wt); GL261 cells, GL DsRed; DsRed expressing GL261 cells after G418 selection, Circle 1; ferritin–DsRed-expressing GL261 cells before G418 selection, Circle 2–6 ferritin–DsRed-expressing GL261 cells after G418 selection.

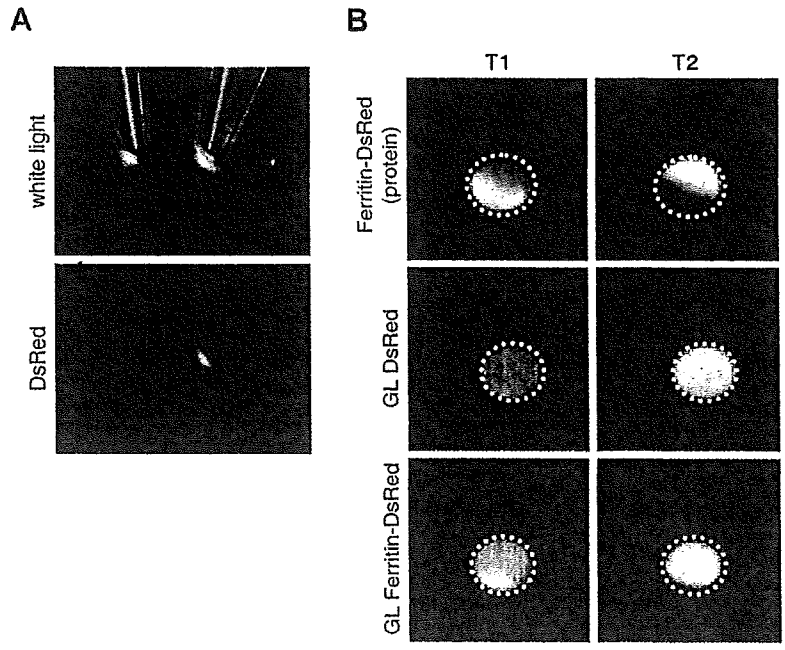

Fig. 2. In vitro optical imaging and MRI of ferritin–DsRed-expressing GL261 cells. Cell pellets from GL261 cells were observed by optical imaging (A) and MRI (B). (A) Left tube was from GL261 cells and right tube was from ferritin–DsRed-expressing GL261 cells. The upper panel indicated a photo exposed to white light and lower panel indicated DsRed fluorescence at the same location. (B) Recombinant protein and cell pellets were acquired for T1-weighted images and T2-weighted images by MRI. Ferritin–DsRed (protein); recombinant ferritin–DsRed fusion protein from *E. coli*, GL DsRed; DsRed-expressing GL261 cells, GL ferritin–DsRed; ferritin–DsRed-expressing GL261 cells, T1; T1-weighted image, T2; T2-weighted image.

MRI. The T2-weighted images indicated a similar dense deposit which meant there was enhanced visualizing effect by reduction of T2-weighted signal intensity for the cell pellet, as ferritin–DsRed fusion protein, but not DsRed expressing GL261 cells. Thus, ferritin expression in GL261 cells was detectable by *in vitro* MRI.

To visualize the reporter transgene expression by *in vivo* MRI, we made a brain tumor model with GL261 cells expressing ferritin–DsRed. At 3 weeks after injection of GL261 cells, mice were analyzed by optical imaging (Fig. 3A). DsRed fluorescence was detected on the right side of the brain, where ferritin–DsRed-expressing GL261 cells were injected. Then, we tried to detect ferritin–DsRed-expressing GL261 cells in the mouse brain, by MRI (Fig. 3B). As the first step to examination, MRI was used to examine a mouse injected with recombinant ferritin–DsRed on the right hemisphere of brain and control protein on the left hemisphere of brain. The T2-weighted images showed a dense core on the right hemisphere due to reduced T2-weighted signal intensity, but no change of signal for the left hemisphere, indicating recombinant ferritin–DsRed could be detected *in vivo*. As a following step, mouse injected with ferritin–DsRed-expressing GL261 cells on the right hemisphere of brain and GL261 cells on the left hemisphere of brain, was observed by MRI. At 3 weeks after injection of GL261 cells, the brain in the T2-weighted image apparently acknowledged for growth of glioma cells, because brain tumors from GL261 cells in the brain increased T2-weighted signal intensity. Photographs of the brain section from the sacrificed mouse were taken and analyzed at the same location of the T2-weighted image (Fig. 3C). The image acquired was fluorescent at the left and right hemispheres of the brain, however, DsRed-specific fluorescence was spectrometrically detected only on the right hemisphere of the brain (Fig. 3C). Since DsRed fluorescence arose from the transplanted GL261 cells expressing ferritin–DsRed, it was confirmed that a dense deposit located around the center of tumor originated from the signal of ferritin–DsRed-expressing cells (Fig. 3D). This was confirmed by a densitometric analysis (Fig. 3D).

Upon preparing the plasmid to express a ferritin reporter for the intracellular domain, we examined whether permeability of iron against plasma membrane affected contrast effects according to ferritin reporter. When permeated ferritin–DsRed-expressing cells were injected into the brain, the contrast was enhanced in T2-weighted images at injected sites, compared to injection of non-permeated cells (Fig. 4A). The immunohistochemical analysis detected many DsRed expressing GL261 cells where the dense deposits were located in the T2-weighted image (Fig. 4B). In

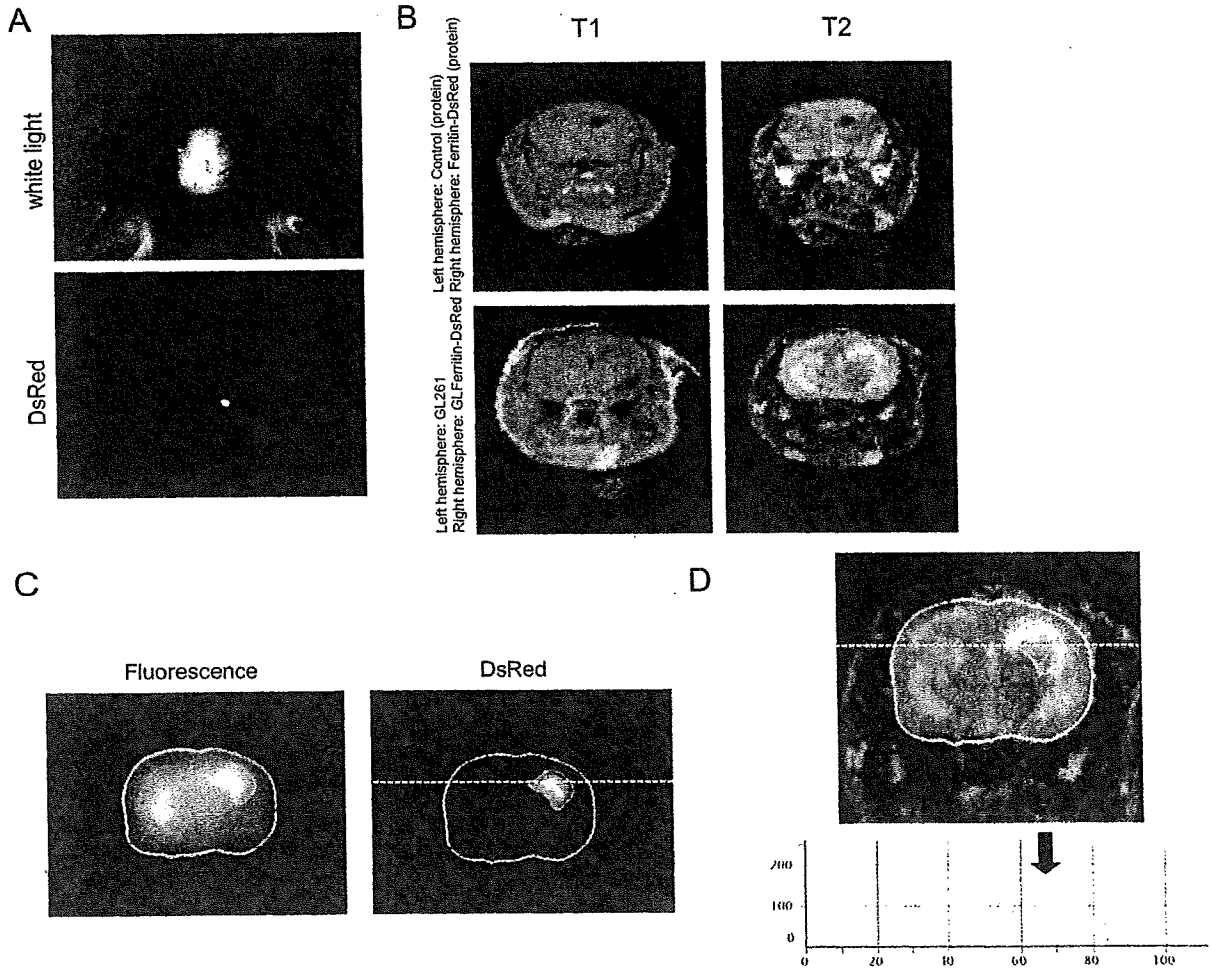

Fig. 3. *In vivo* optical imaging and MRI for ferritin–DsRed-expressing GL261 cells in the brain tumor model. Mouse brain transplanted GL261 cells, were observed by optical imaging (A) and MRI (B). (A) Upper panel indicates a photo exposed to white light and lower panel indicates DsRed fluorescence at the same location. (B) Upper panels showed T1-weighted and T2-weighted images in the brain just after injection of control protein (Left brain) and recombinant ferritin–DsRed (Right brain), and lower panels showed the images in the brain at 3 weeks after injection of control GL261 cells (Left brain) and ferritin–DsRed-expressing GL261 cells (Right brain). A brain section (C) was observed by optical imaging in the same location as MRI images in B. The outline of the brain section and the edge of brain tumor from ferritin–DsRed-expressing GL261 cells was drawn with a white solid line. (D) T2-weighted image (shown in B) overlaid with the white solid line (shown in C). The histogram showed signal intensity with a white dashed straight line in the T2-weighted image and the arrow indicated intensity reduced due to ferritin effect.

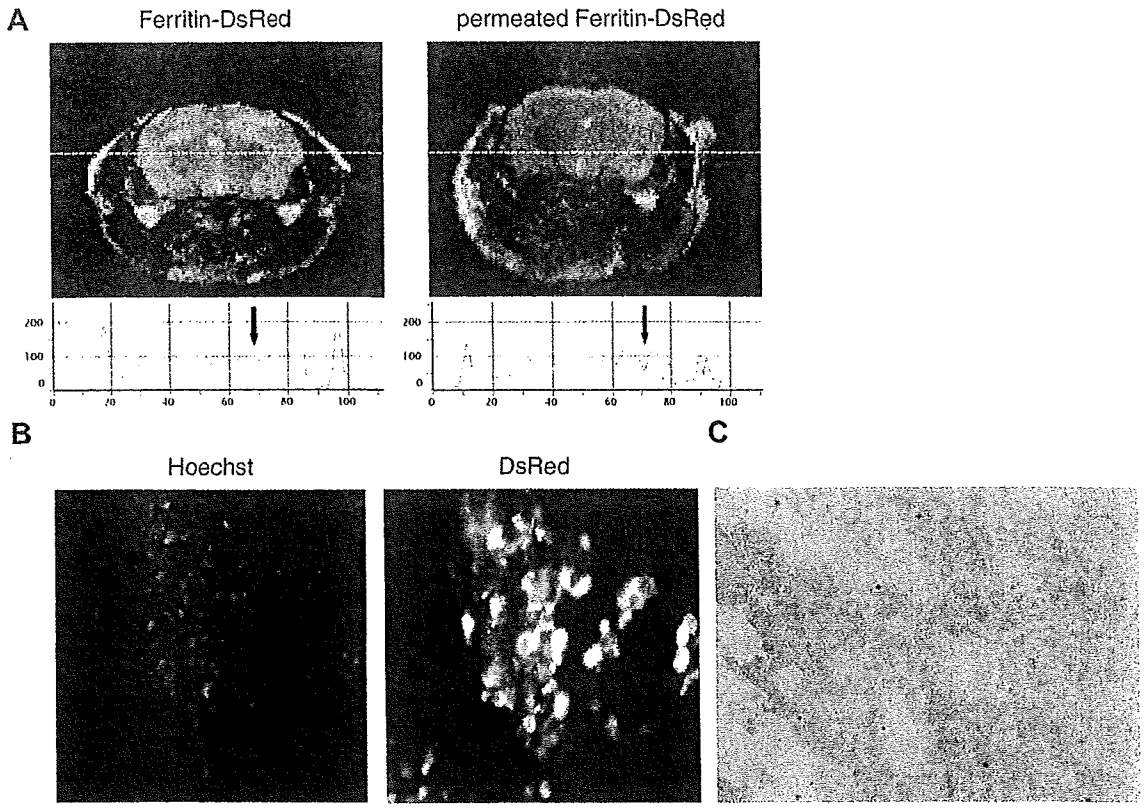

Fig. 4. Contrast effect of ferritin reporter in MRI when membrane permeability of GL261 cells increased. T2-weighted images were shown in (A) when ferritin–DsRed-expressing GL261 cells or the permeated GL261 cells were injected into the mouse right brain. Histograms showed signal intensity on the white dashed straight line and the arrow indicated location of injected GL261 cells. Brain sections from mice injected with permeated cells, were confirmed of DsRed expression (B) by immunohistochemical staining and iron binding (C) by Berlin blue staining.

addition, a lot of iron molecules were located in these cells in brain parenchyma (Fig. 4C).

Discussion

Common consensus was that it was difficult to detect change in gene expression using MRI, as compared to optical imaging. This is because optical imaging using fluorescent protein, such as GFP and DsRed or chemiluminescence with luciferase enzymes, was the common choice. In this study, we particularly focused on the iron effect of reducing the high T2-weighted signal intensity of normal tissue in MRI [2], and studied ferritin molecules where one molecule can bind to 4500 iron atoms at maximum [7]. We successfully chased gene-transfected cells in the brain in our MRI studies using ferritin molecules as a reporter under β-actin promoter control. Since it is easy to convert DsRed to other proteins, this system will be able to chase many protein expressions for both *in vitro* and *in vivo* MRI studies. In addition, this reporter system can also be applied for various cells since the promoter region also changed from a β-actin promoter to other gene promoters, and ferritin molecules can be expressed in intracellular organelles and plasma membranes, as well as cytoplasm.

This study demonstrated that it was possible to visualize gene expression in T2-weighted images for MRI by reducing the high T2-weighted signal intensity in animal tissues with intracellular expression of ferritin. In addition, it was found that there was higher cell permeation against iron enhanced visualizing effect of ferritin, compared to non-permeated cells. This suggests it may be possible to achieve more significant signal visualizing effect, by creating a microenvironment where iron atoms and ferritin molecules can easily bind. Transferrin receptors play an important role in transporting iron from extracellular fluid to intracellular fluid [10]. Therefore, co-expression of transferrin receptors with ferritin molecules may efficiently be improved by reducing signal intensity in T2-weighted images for MRI. Morever, it may be possible to effectively improve visualizing effect with ferritin expression in the extracellular domain of the plasma membrane, instead of the cytoplasm. When compared to the DsRed expressing GL261 cells as a control, we found that ferritin–DsRed-expressing GL261 cells showed low or medium DsRed fluorescence. This indicates that ferritin–DsRed fusion protein expression is less than DsRed. However, it is still unknown whether the expression level is lower due to fusion protein molecular weight or structure that may have affected stability and/or toxicity. Since other studies have reported that overexpression of ferritin alleviated cell damage [11,12], it may not be about cytotoxicity. Further studies will clarify stability and cytotoxicity of over-expressed ferritin molecules.

MRI is a useful and safe clinical diagnostic tool since it doesn't use radiation to get high resolution tomographic images. MRI is also used to monitor blood flow rate with fMRI [13] or gadolinium contrast reagents [14], however, it has not been a technique useful for gene expression imaging. This was due to lack of precise reporters to chase protein expression of the gene expression [15]. Based on our results, use of the ferritin reporter system is expected to expand possibilities to diagnose gene expression using MRI.

Acknowledgments

This study was supported by the Research for Promoting Technological Seeds from Japan Science and Technology Agency and Indus-

trial Technology Research Grant Program from the New Energy and Industrial Technology Development Organization (NEDO) of Japan.

References

[1] G.D. Luker, K.E. Luker, Optical imaging: current applications and future directions, J. Nucl. Med. 49 (2008) 1–4.
[2] J.T. Ferrucci, D.D. Stark, Iron oxide-enhanced MR imaging of the liver and spleen: review of the first 5 years, Am. J. Roentgenol. 155 (1990) 943–950.
[3] R.A. Panizzo, P.G. Kyrtatos, A.N. Price, D.G. Gadian, P. Ferretti, M.F. Lythgoe, In vivo magnetic resonance imaging of endogenous neuroblasts labelled with a ferumoxide–polycation complex, Neuroimage 44 (2009) 1239–1246.
[4] K. Imam, D.A. Bluemke, MR imaging in the evaluation of hepatic metastases, Magn. Reson. Imaging Clin. N. Am. 8 (2000) 741–756.
[5] S. Hirohashi, H. Uchida, K. Yoshikawa, N. Fujita, K. Ohtomo, Y. Yuasa, Y. Kawamura, O. Matsui, Large scale clinical evaluation of bowel contrast agent containing ferric ammonium citrate in MRI, Magn. Reson. Imaging 12 (1994) 837–846.
[6] B. Cohen, K. Ziv, V. Plaks, T. Israely, V. Kalchenko, A. Harmelin, L.E. Benjamin, M. Neeman, MRI detection of transcriptional regulation of gene expression in transgenic mice, Nat. Med. 13 (2007) 498–503.
[7] E.C. Theil, Ferritin: at the crossroads of iron and oxygen metabolism, J. Nutr. 133 (2003) 1549S–1553S.
[8] C. Ferreira, D. Bucchini, M.E. Martin, S. Levi, P. Arosio, B. Grandchamp, C. Beaumont, Early embryonic lethality of H ferritin gene deletion in mice, J. Biol. Chem. 275 (2000) 3021–3024.
[9] Z. Gottesfeld, M. Neeman, Ferritin effect on the transverse relaxation of water: NMR microscopy at 9.4 T, Magn. Reson. Med. 35 (1996) 514–520.
[10] A.E. Deans, Y.Z. Wadghiri, L.M. Bernas, X. Yu, B.K. Rutt, D.H. Turnbull, Cellular MRI contrast via coexpression of transferrin receptor and ferritin, Magn. Reson. Med. 56 (2006) 51–59.
[11] M. Festa, G. Ricciardelli, G. Mele, C. Pietropaolo, A. Ruffo, A. Colonna, Overexpression of H ferritin and up-regulation of iron regulatory protein genes during differentiation of 3T3-L1 pre-adipocytes, J. Biol. Chem. 275 (2000) 36708–36712.
[12] A. Cozzi, B. Corsi, S. Levi, P. Santambrogio, A. Albertini, P. Arosio, Overexpression of wild type and mutated human ferritin H-chain in HeLa cells: in vivo role of ferritin ferroxidase activity, J. Biol. Chem. 275 (2000) 25122–25129.
[13] E.A. DeYoe, P. Bandettini, J. Neitz, D. Miller, P. Winans, Functional magnetic resonance imaging (FMRI) of the human brain, J. Neurosci. Methods 54 (1994) 171–187.
[14] G.L. Wolf, Current status of MR imaging contrast agents: special report, Radiology 172 (1989) 709–710.
[15] R. Weissleder, A clearer vision for in vivo imaging, Nat. Biotechnol. 19 (2001) 316–317.

Ann Nucl Med (2010) 24:163–169
DOI 10.1007/s12149-009-0339-0

ORIGINAL ARTICLE

Two activated stages of microglia and PET imaging of peripheral benzodiazepine receptors with [^{11}C]PK11195 in rats

Fumitaka Ito · Hiroshi Toyama · Gen Kudo · Hiromi Suzuki · Kentaro Hatano · Masanori Ichise · Kazuhiro Katada · Kengo Ito · Makoto Sawada

Received: 2 September 2009 / Accepted: 8 December 2009 / Published online: 26 January 2010

Abstract

Objective The transition of microglia from the normal resting state to the activated state is associated with an increased expression of peripheral benzodiazepine receptors (PBR). The extent of PBR expression is dependent on the level of microglial activation. A PBR ligand, [^{11}C]PK11195, has been used for imaging of the activation of microglia in vivo. We evaluated whether [^{11}C]PK11195 PET can indicate differences of microglial activation between no treatment and lipopolysaccharide (LPS) treatment in a rat artificial injury model of brain inflammation.

Methods On day 1, a small aliquot of absolute ethanol was injected into the rat right striatum (ST) to produce artificial brain injury. On day 3, MRI scans were performed to evaluate and select rats showing a similar degree of brain injury. Then LPS or vehicle was administered intraperitoneally. On day 4, PET scans were performed after a bolus injection of [^{11}C]PK11195. Eleven rats (7 LPS administered rats, 4 LPS non-administered rats) were evaluated. We used uptake ratios of the integral of right and left striatum from 0 to 60 min as an estimate of PBR distribution volume (V_{60}). The number of activated microglia and mRNA expression of inflammatory cytokines (TNFα, IL-1β) were assessed by isolectin-B4 staining and RT-PCR, respectively.

Results Right/left ST V_{60} ratios of LPS group were significantly higher than those of non-LPS group ($P < 0.03$). Although there were no significant differences in the number of activated microglia between the two groups, LPS group showed higher expression of inflammatory cytokines (TNFα, IL-1β) than the non-treated group indicating that further activation was induced by LPS treatment.

Conclusion The results suggest that intensity of PBR signals in [^{11}C]PK11195 PET may be related to the level of microglial activation rather than the number in activated microglia at least in an artificial brain injury model.

Keywords Peripheral benzodiazepine receptor · Animal PET · Activated microglia · Toxic conversion · Lipopolysaccharide

F. Ito (✉) · H. Toyama · G. Kudo · K. Katada
Department of Radiology, Fujita Health University,
1-98 Dengakugakubo, Kutsukake, Toyoake
Aichi 470-1192, Japan
e-mail: fito@fujita-hu.ac.jp

H. Suzuki · M. Sawada
Department of Brain Function,
Research Institute of Environmental Medicine,
Nagoya University, Nagoya, Japan

K. Hatano · K. Ito
Department of Brain Science and Molecular Imaging,
National Institute for Longevity Science, National Center
for Geriatrics and Gerontology, Obu, Japan

M. Ichise
Department of Radiology, Columbia University,
New York, NY, USA

Introduction

Microglia are central nervous system cells having various properties, such as control of neuronal activity and homeostasis, and release of neurotrophic and neurotoxic factors including nitric oxide, cytokines, and neurotrophins. Microglia convert to activated forms when diseases cause neuronal degeneration and the activated microglia accumulate in the affected areas [1], a portion of which proliferates in response to the appropriate intercellular

signaling. Histopathologically, microglial activation begins from several hours and lasts for several days after disease onset [2, 3]; this early microglial activation appears to be an important factor for the formation of various brain lesions seen in several neurodegenerative diseases, brain infarction, and brain tumors. Several lines of evidence suggest that there are some functional differences in activated microglia; some of them indicate cytotoxic properties, which produce several toxic materials to eliminate damaged cells beyond the point of recovery, while others indicate rather protective characteristics, which release neurotrophic factors and protect cells from damage [4, 5]. The former state of activated microglia is sometimes referred to as a 'further activated' or 'fully activated' form. These two different characteristics of activated microglia play an important role in the pathophysiology of common disorders, such as Alzheimer's disease and Parkinson's disease. It is worth distinguishing between the two different activated states of microglia for the diagnosis of brain diseases and possibly for planning further treatment strategies. However, there is no reliable in vivo method to evaluate the contribution of different states of activated microglia to the disease process.

Microglial activation has been shown to increase the expression of peripheral benzodiazepine receptors (PBR) that are located on the mitochondrial membrane of the microglia [6]. PBR is a widely distributed transmembrane protein that is located mainly in the outer mitochondrial membrane. Many functions are associated with the PBR, including regulation of cholesterol transport and synthesis of steroid hormones, porphyrin transport, and heme synthesis. Recently, PBR has been renamed as "translocator protein (18 kDa)" due to recent data regarding the structure and molecular function of this protein [7].

[^{11}C]PK11195 is a PET radioligand used to image PBR. This ligand can be easily labeled with a positron emitter, crosses the blood-brain barrier and binds reversibly to the central PBR. However, because of relatively low affinity of [^{11}C]PK11195 for PBR [8–10], the target to background ratio is relatively low [11] compared to newly developed ligands [12–14] and the biological significance of [^{11}C]PK11195 in terms of microglial activation has not been fully investigated. We showed previously that activated microglia in a rat model of brain inflammation induced by ethanol microinjection accumulate in the damaged area and that microglial activation resulted in a significant increase in the [^{11}C]PK11195 signal in vivo [15].

In the present study, we experimentally induced the two different states of activated microglia and evaluated the level of activated states with [^{11}C]PK11195 PET imaging of PBR in rats.

Materials and methods

The experimental procedures are described in chronological order as below.

Animal model preparation

All procedures were conducted in accordance with the guidelines of the National Institutes of Health and Animal Experimentation of Fujita Health University, School of Medicine. The study protocol was approved by the Animal Experimentation Ethics Committee of the National Center for Geriatrics and Gerontology.

Using 9-week-old male Wistar rats weighing 280–300 g (Nihon Charles River, Tokyo, Japan), general anesthesia was induced by administering pentobarbital (50 mg/kg). After immobilizing the head using a brain stereotactic apparatus (Narishige, Tokyo, Japan), an incision was placed on the scalp to expose the skull. Using a bone drill, a hole was made in the skull to an area that was 0.4 mm anterior, 3 mm lateral, and 4.5 mm ventral to the bregma (point on the skull where the coronal and sagittal sutures converge), and using a 10-μl Hamilton syringe, 8 μl of ethanol was injected to the right striatum to cause brain injury [3].

MRI imaging

After preparing the artificial brain injury model, stereotactic MRI imaging was performed to identify the location of the brain injury, and the severity of the brain injury in the rat striatum was assessed on T1-weighted, T2-weighted, and Gd-DTPA enhanced T1-weighted images. Gd-DTPA enhanced T1-weighted images were used to confirm the presence or absence of the destruction of the blood-brain barrier due to ethanol injection to the right striatum.

We performed the following PET scanning with and without LPS injections only for injured rats showing almost the same extent of high intensity area around the ethanol injected right striatum on the T2 weighted images (Fig. 1).

For MRI scanning, the Signa Infinity Excite (1.5 T, GE Healthcare, Milwaukee, USA) and a wrist coil (Q-WRIST, GE Healthcare, Milwaukee, USA) were used.

LPS treatment

Just after the MRI scanning, to induce further activation of microglia, LPS (SIGMA-ALDRICH, Saint Luis, USA) was injected intraperitoneally (10 mg/kg) to seven out of eleven rats (LPS group), and vehicle was injected to the others (non-LPS group).

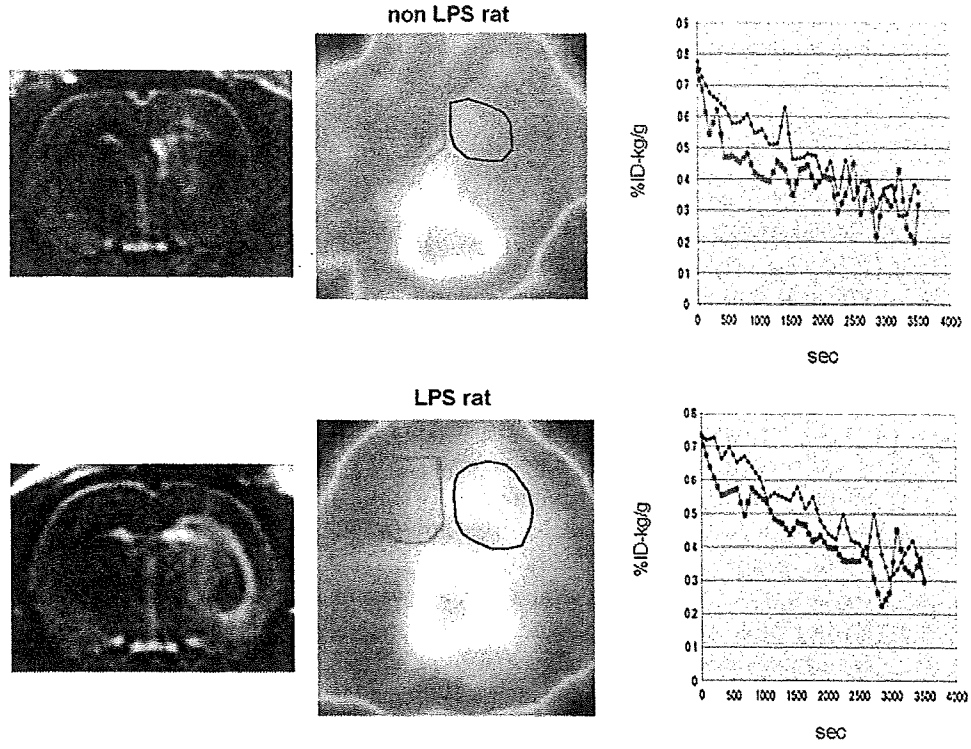

Fig. 1 Representative coronal MRI T2 weighted images (*left column*), summed images (0–60 min) and time-activity curves (injured right and non-injured left striatum) of [^{11}C]PK-11195 in ethanol injury rats for a non-LPS rat (*upper row*) and an LPS rat (*lower row*). The ROIs are placed in bilateral striata on the [^{11}C]PK-11195 images. *Blue lines* show injured right striatum and *pink lines* show non-injured left striatum. LPS rat shows much slower clearance in injured right striatum as compared with non-injured left striatum than in non-LPS rat

PET imaging

Using the method reported by Sakiyama et al. [16] and our group [15], anesthesia was induced by intraperitoneally administering chloral hydrate (300 mg/kg), and the head of each rat was fixed using an acrylic brain stereotactic device (Hamamatsu Photonics, Hamamatsu, Japan). To prevent anesthesia-induced hypothermia, a heat mat was placed under the rat to maintain its rectal temperature at 37.0 ± 0.5°C. PET was performed using an animal PET scanner (SHR-2000, Hamamatsu Photonics, Hamamatsu, Japan, spatial resolution: 3.5 mm FWHM). Under general anesthesia induced by infusing chloral hydrate through the tail vein (100 mg/kg/h), 39–64 MBq of [^{11}C]PK11195 was administered intravenously as a bolus, and PET was immediately performed for 60 min (1 min/frame).

PET data analysis

PET images were analyzed using our previously reported method [15]. With small rat brain and limited number of voxels involved, rather than cluster analysis as used by the Hammersmith hospital group [17–19] or reference tissue models [20, 21], we sought to estimate a more direct measure of PBRs receptor binding by an ROI-based approach to estimate the distribution volume.

Based on our previously reported method [15], regions of interest (ROIs) were established on the cross-sectional stereotactic [^{11}C]raclopride PET image which was performed previously for template at the level of the bilateral striata. Guided by these [^{11}C]raclopride striatal ROIs, ROIs were placed for the bilateral striata on stereotactic [^{11}C]PK11195 PET images.

As reported previously [15], PBR binding was estimated by calculating the ipsi- to contra-lateral area ratio of the time-activity curve (TAC).

Intracerebral distribution volume (V) was defined as follows [22]:

$$V = \frac{\int_0^{\infty} \mathrm{ROI}\, dt}{\int_0^{\infty} \mathrm{Plasma}\, dt}.$$

In this study, V was approximated as the area under the curve (AUC) ratio from minutes 0 to 60 min (V_{60}).

The ratio of the V_{60} for the right striatum with brain injury (RST) to that for the left striatum without injury (LST) was calculated as follows:

$$V_{60}\,(\mathrm{RST})/V_{60}(\mathrm{LST}) = (\mathrm{RST\ AUC/plasma\ AUC})/(\mathrm{LST\ AUC/plasma\ AUC}) = \mathrm{RST\ AUC/LST\ AUC}.$$

The calculation of the above V_{60} ratios actually did not require plasma data because the plasma AUC term cancels out in the above equation. An unpaired t test was used to

compare the LPS and non-LPS groups with the level of significance set at $P < 0.05$.

Histochemical assessment of activated microglia

After PET imaging, additional anesthesia was accomplished by administering pentobarbital (50 mg/kg) intraperitoneally, and after transcardial perfusion using 0.01 M PBS (pH: 7.4), the brain tissue was removed. Excised fresh brain tissue was mounted using an OCT compound (Dako Cytomation, Carpinteria, USA) and quickly frozen, and then 10-μm sections were prepared using a cryostat and placed on gelatin-coated slide glass. After fixing brain tissue sections using 4% paraformaldehyde/0.1 M phosphate buffer at room temperature for 10 min, microglia were stained using biotin-labeled isolectin-B4 (IB4) [23].

Biotin-labeled IB4 (SIGMA-ALDRICH, Saint Louis, USA) was diluted to 2 μg/μl and was allowed to react at 4°C for 24 h. After washing with PBS, streptoavidin–HRP conjugate reagent (KPL, Gaithersburg, USA) was labeled at room temperature for 30 min, and 3,3′-diaminobenzidine tetrahydrochloride (DAB, Vector Lab., Burlingame, USA) was used for the detection at room temperature for 10 min. After DAB, hematoxylin was used for nuclear staining.

After staining, a virtual microscope Aperio (Aperio Technologies, Viata, USA, microscope-incorporated line-scan slide glass scanner) was used to histologically quantify the number of IB4-positive activated microglia in the left and right striata with ImagePro software which allows automatic threshold setting in relation to background data. For each rat, the results of five sections were averaged. An unpaired t test was used to compare the LPS and non-LPS groups with the level of significance set at $P < 0.05$.

Evaluation of the extent of microglial activation by examining the inflammatory cytokines

Using adjacent frozen brain sections to the sections used in immunohistological analysis, total RNA was extracted to assess the mRNA expression of inflammatory cytokines, TNFα, and Il-1β, by RT-PCR for a marker of activated microglia. Rat brain tissue was sliced into 10-μm sections, and 15 sections were placed in 1.5-ml plastic tubes. Lysis buffer composed of RLT buffer and 2-mercaptoethanol (B-ME, SIGMA-ALDRICH, Saint Louis, USA) was added, and the tissue sections were crushed. The RNeasy total RNA isolation kit (QIAGEN, Valencia, USA) was used for RNA extraction, and using 1 μg of total RNA, RT-PCR was performed using the previously reported method [24]. After PCR, products were analyzed by electrophoresis using ethidium bromide stained 2% agarose gel, and then quantified with ATTO coolserver software (ATTO, Tokyo, Japan).

Results

Histochemical assessment of activated microglia by comparison of numbers of activated microglia between injured and non-injured striata

When compared to the non-injured left striatum, IB4-positive activated microglial accumulation was observed around the injured right striatum, and activated microglia exhibited an ameboidal shape (Fig. 2). Marked tissue loss was seen in the injured striatum for the LPS group (Fig. 3-1) suggesting that further activation of microglia was induced by LPS treatment. However, both with and without LPS administration, numerous ameboidal shape IB4-positive microglia were observed in injured striatum (Fig. 3-1), and there were no significant differences in the number of IB4-positive activated microglia between the two groups (Fig. 3-2).

Assessment of the level of microglial activation by inflammatory cytokine expression

The amount of expression of inflammatory cytokine mRNA is dependent on the extent of activated microglia. So, TNFα and IL-1β mRNA expression was compared between the LPS and non-LPS groups. The expression of TNFα and IL-1β in the LPS rats was greater (Fig. 4-1) than that in the non-LPS treated rats.

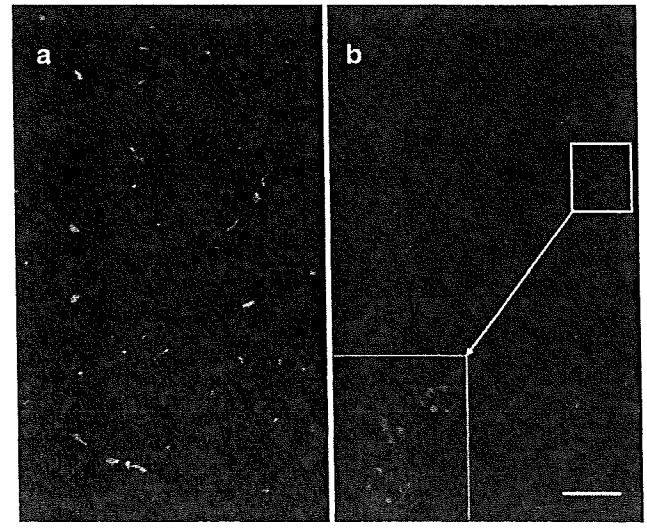

Fig. 2 Immunohistochemical staining (Isolectin-B4 stain) on the ethanol-injured right and non-injured left striatum in the same lesioned rat model (*Bar* 10 μm). Microglial accumulation is not seen in non-injured striatum (**a**). Ameboidal activated microglial accumulation is seen around the injured striatum (**b**)

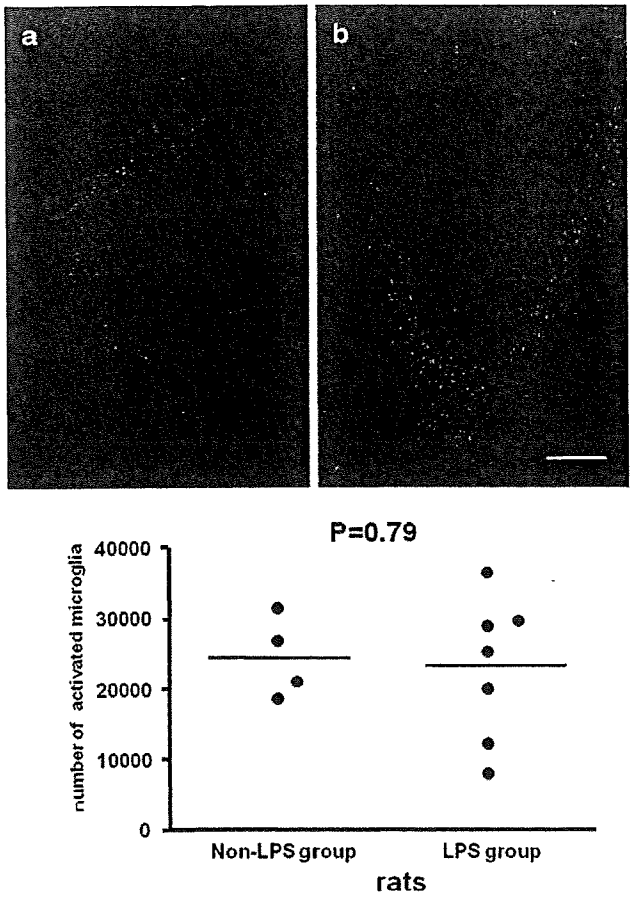

Fig. 3 1 Effects of intraperitoneal LPS administration on the ethanol injury model. When compared to the non-LPS rat (**a**), marked tissue loss is seen in the LPS rat (**b**), and microglial accumulation is seen around the ethanol-injured striatum. Isolectin-B4 was used for histological staining (*Bar* 10 μm) 2 Comparison of number of activated microglial cells in the injured striatum of the ethanol injury model between LPS and non-LPS group. No significant differences are seen in the number of activated microglial cells between the two groups

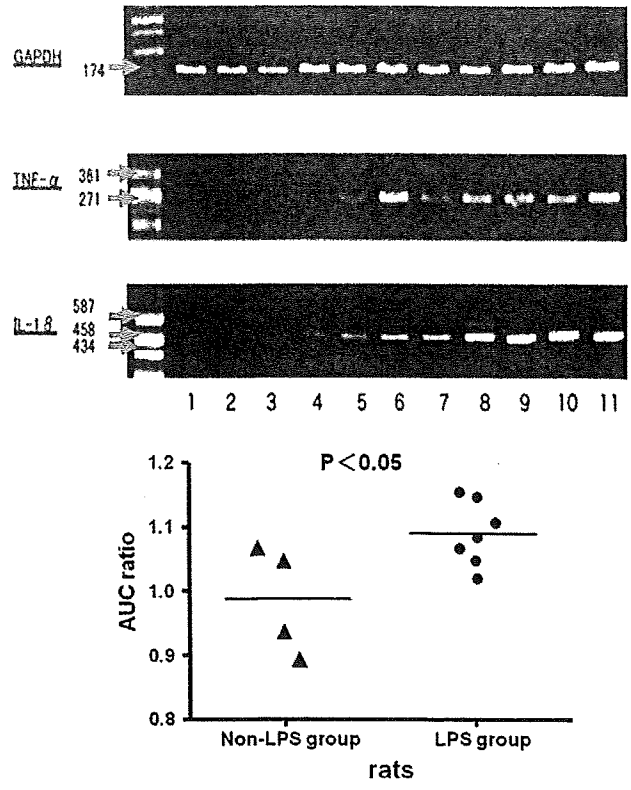

Fig. 4 1 Expression of inflammatory cytokines in the ethanol injury model. All LPS group rats show intense increased expressions both in TNFα and in IL-1β (*lanes 5–11*). However, non-LPS group rats show mildly increased expression both in TNFα and in IL-1β (*lanes 1–4*). TNFα rat primer: product size 289 Fw5′-GCCTCAGCCTCTTCT GAT-3′, Bw5′-ACCAGTTGGTTGTCTTTG-3′, IL-1β rat primer: product size 467, Fw5′-CGACAGTGAGGAGAATGA-3′, Bw5′-CGTTGCTTGTCTCTCCTT-3′, GAPDH rat primer: product size 174, Fw5′-TGCACCACCAACTGCTTA-3′, Bw5′-GATGCAGGG ATGATGTTC-3′. 2 The ethanol-injured right to non-injured left striatum region ratio of the area under the time-activity curve (AUC) of the ^{11}C-PK11195 dynamic PET. The AUC ratio for the LPS group is significantly greater than that for the non-LPS group

Comparison of PBR signal in [^{11}C]PK11195 PET

The AUC ratio for the LPS group was 1.09 ± 0.05, which was significantly greater than that for the non-LPS group at 0.99 ± 0.05 ($P < 0.05$; Fig. 4-2).

Summed images and time-activity curves of [^{11}C]PK11195 PET in representative LPS and non-LPS rats are shown in Fig. 1.

Discussion

In the present study, we experimentally induced the two different states of activated microglia and evaluated the level of activated states with PET imaging of PBR in rats. We found that intensity of PBR signals in [^{11}C]PK11195 PET may be related to level of microglial activation rather than number in activated microglia at least in an artificial brain injury model.

There was a marked neuronal degeneration for the LPS group around the artificially damaged striatum and activated microglia accumulated around the ipsilateral striatum. Sawada et al. [3] found that intraperitoneal administration of LPS increased the size of artificial injury and the number of damaged nerve fibers around the injury, as detected by FluoroJadeB (unpublished observation). In the brain injury model which we used in this experiment, peripheral inflammatory cells do not contribute to brain inflammation and damage as reported previously. Thus, IB4-positive cells reflect the activation of endogenous microglia in this brain injury model [3]. Therefore, the difference in the histological findings that marked tissue loss was seen in the damaged striatum of the LPS group

should be related to further activation of microglia that were induced by LPS administration.

Hardwick et al. [25] reported the increased [^{11}C]PK11195 accumulation in the lungs of LPS-treated mice on in vivo small animal PET studies. Venneti et al. [26] demonstrated that [^{3}H](R)-PK11195 binding was increased in activated macrophages using post mortem tissues from macaques' encephalitis with simian immunodeficiency virus infection and also macrophage cultures treated with LPS. In this report we indicated that increased [^{11}C]PK11195 uptake in animal PET correlates with the extent of microglial activation in the brain after LPS administration. We observed that LPS administration markedly increased the expression of inflammatory cytokines (Fig. 4-1), indicating that additional activation of microglia was induced by LPS treatment; this state of the activation might be correlated with toxic state of microglial activation since damage severity was marked in LPS-treated brain. It is possible that peripherally administered LPS could activate cerebral microglia to induce the expression of inflammatory cytokines as reported previously [4]. In spite of increase of inflammatory cytokine expression, no significant differences were observed in the total number of activated microglia in the artificially damaged striatum between the LPS and non-LPS groups (Fig. 3-2). These results suggest that LPS administration caused further activation of microglia located at the surrounding area in the injured striatum. Accompanied with the histological observation and PCR analysis, this activated state may relate to the toxic form of activated microglia. We should address that PBR expression is actually amplified by toxic conversion of activated microglia.

Conclusions

The results suggest that intensity of PBR signals in [^{11}C]PK11195 PET may be related to level of microglial activation rather than number in activated microglia at least in an artificial brain injury model.

Acknowledgments We would like to thank Mr. Junichiro Abe, Department of Brain Science and Molecular Imaging, National Institute for Longevity Sciences, National Center for Geriatrics and Gerontology, Obu, Japan for running cyclotron. We appreciate radiological technologists, Fujita Health University Hospital for running the MRI scanner. We also thank Eizou Umezawa, PhD, School of Health Sciences, Fujita Health University for providing support with regard to statistical analysis. This study was supported by Japan Society for the Promotion of Science (JSPS) KAKENHI (18591369, 80001800), the 21st Century COE (Center of Excellence) Medical Program (Development Center for Targeted and Minimally Invasive Diagnosis and Treatment) from JSPS, and a grant from Fujita Health University.

References

1. Kreutzberg GW. Microglia: a sensor for pathological events in the CNS. Trends Neurosci. 1996;19:312–8.
2. Banati RB. Neuropathological imaging: in vivo detection of glial activation as a measure of disease and adaptive change in the brain. Br Med Bull. 2003;65:121–31.
3. Takeuchi A, Isobe K, Miyaishi O, Sawada M, Fan ZH, Nakashima I, et al. Microglial NO induces delayed neuronal death following acute injury in the striatum. Eur J Neurosci. 1998;10:1613–20.
4. Sawada M, Suzumura A, Marunouchi T. Cytokine network in the central nervous system and its roles in growth and differentiation of glial and neuronal cells. Int J Dev Neurosci. 1995;13:253–64.
5. Sawada M, Sawada H, Nagatsu T. Effects of aging on neuroprotective and neurotoxic properties of microglia in neurodegenerative diseases. Neurodegener Dis. 2008;5:254–6.
6. Banati RB, Egensperger R, Maassen A, Hager G, Kreutzberg G, Graeber MB. Mitochondria in activated microglia in vitro. J Neurocytol. 2004;33:535–41.
7. Papadopoulos V, Baraldi M, Guilarte TR, Knudsen TB, Lacapere JJ, Lindemann P, et al. Translocator protein (18 kDa): new nomenclature for the peripheral-type benzodiazepine receptor based on its structure and molecular function. Trends Pharmacol Sci. 2006;27:402–9.
8. Vowinckel E, Reutens D, Becher B, Verge G, Evans A, Owens T, et al. PK11195 binding to the peripheral benzodiazepine receptor as a marker of microglia activation in multiple sclerosis and experimental autoimmune encephalomyelitis. J Neurosci Res. 1997;50:345–53.
9. Debruyne JC, VanLaere KJ, Versijpt J, DeVos F, Eng JK, Strijckmans K, et al. Semiquantification of the peripheral-type benzodiazepine ligand [^{11}C]PK11195 in normal human brain and application in multiple sclerosis patients. Acta Neurol Belg. 2002;102:127–35.
10. Zhang MR, Maeda J, Ogawa M, Noguchi J, Ito T, Obayashi S, et al. Development of a new radioligand, *N*-(5-fluoro-2-phenoxyphenyl)-*N*-(2-[^{18}F]fluoroethyl-5-methoxybenzyl) acetamide, for PET imaging of peripheral benzodiazepine receptor in primate brain. J Med Chem. 2004;47:2228–35.
11. Groom GN, Junck L, Foster NL, Frey KA, Kuhl DE. PET of peripheral benzodiazepine binding sites in the microgliosis of Alzheimer's disease. J Nucl Med. 1995;36:2207–10.
12. Maeda J, Higuchi M, Inaji M, Ji B, Haneda E, Okauchi T, et al. Phase-dependent roles of reactive microglia and astrocytes in nervous system injury as delineated by imaging of peripheral benzodiazepine receptor. Brain Res. 2007;1157:100–11.
13. Venneti S, Lopresti BJ, Wang G, Slagel SL, Mason NS, Mathis C, et al. A comparison of the high-affinity peripheral benzodiazepine receptor ligands DAA 1106 and (R)-PK11195 in rat models of neuroinflammation: implications for PET imaging of microglial activation. J Neurochem. 2007;102:2118–31.
14. Imaizumi M, Kim H-J, Zoghbi SS, Briard E, Hong J, Musachio JL, et al. PET imaging with [^{11}C]PBR28 can localize and quantify upregulated peripheral benzodiazepine receptors associated with cerebral ischemia in rat. Neurosci Lett. 2007;411:200–5.
15. Toyama H, Hatano K, Suzuki H, Ichise M, Momosaki S, Kudo G, et al. In vivo imaging of microglial activation using a peripheral benzodiazepine receptor ligand: [^{11}C]PK-11195 and animal PET following ethanol injury in rat striatum. Ann Nucl Med. 2008;22:417–24.
16. Sakiyama Y, Hatano K, Kato T, Tajima T, Kawasumi Y, Ito K. Stimulation of adenosine A1 receptors decreases in vivo dopamine D1 receptor binding of [^{11}C]SCH23390 in the cat striatum

revealed by positron emission tomography. Ann Nucl Med. 2007;21:447–53.
17. Banati RB. Visualizing microglial activation in vivo. Glia. 2002;40:206–17.
18. Cagnin A, Brooks DJ, Kennedy AM, Gunn RN, Myers R, Turkheimer FE, et al. In vivo measurement of activated microglia in dementia. Lancet. 2001;358:461–7.
19. Gunn RN, Lammertsma AA, Hume SP, Cunningham VJ. Parametric imaging of ligand-receptor interactions using a reference tissue model and cluster analysis. In: Carson R, Daule M, Witherspoon P, Herscovitch P, editors. Quantitative functional brain imaging with positron emission tomography. San Diego: Academic Press; 1998. p. 401–6.
20. Kropholler MA, Boellaard R, Schuitemaker A, Folkersma H, van Berckel BNM, Lammertsma A. Evaluation of reference tissue models for the analysis of [^{11}C](R)-PK11195 studies. J Cereb Blood Flow Metab. 2006;26:1431–41.
21. Schuitemaker A, van Berckel BNM, Kropholler MA, Veltman DJ, Scheltens P, Jonker C, et al. SPM analysis of parametric (R)-[^{11}C]-PK11195 binding images: plasma input versus reference tissue parametric methods. NeuroImage. 2007;35:1473–9.
22. Lassen NA. Neuroreceptor quantitation in vivo by the steadystate principle using constant infusion or bolus injection of radioactive tracers. J Cereb Blood Flow Metab. 1992;12:709–16.
23. Streit WJ. An improved staining method for rat microglial cells using the lectin from Griffonia simplicifonia (GSA I-B4). J Histochem Cytochem. 1990;38:1683–6.
24. Suradhat S, Thanawongnuwech R, Poovorawan Y. Upregulation of IL-10 gene expression in porcine peripheral blood mononuclear cells by porcine reproductive and respiratory syndrome virus. J Gen Virol. 2003;84:453–9.
25. Hardwick MJ, Chen MK, Baidoo K, Pomper MG, Guilarte TR. In vivo imaging of PBRs in mouse lungs: a biomarker of inflammation. Mol Imaging. 2005;4:432–8.
26. Venneti S, Wang G, Wiley CA. Activated macrophages in HIV encephalitis and a macaque model show increased [^{3}H](R)-PK11195 binding in a PI3-kinase-dependent manner. Neurosci Lett. 2007;426:117–22.

Biomaterials 31 (2010) 4094–4103

Contents lists available at ScienceDirect

Biomaterials

journal homepage: www.elsevier.com/locate/biomaterials

Quantum dots labeling using octa-arginine peptides for imaging of adipose tissue-derived stem cells

Hiroshi Yukawa [a,*], Yukimasa Kagami [b], Masaki Watanabe [b], Koichi Oishi [a], Yoshitaka Miyamoto [a], Yukihiro Okamoto [b,c], Manabu Tokeshi [b,c], Noritada Kaji [b], Hirofumi Noguchi [d], Kenji Ono [e], Makoto Sawada [e], Yoshinobu Baba [b,c,f,g,h], Nobuyuki Hamajima [i], Shuji Hayashi [a]

[a] Department of Advanced Medicine in Biotechnology and Robotics, Nagoya University Graduate School of Medicine, Nagoya University, Higashi-ku, Nagoya 461-0047, Japan
[b] Department of Applied Chemistry, Nagoya University Graduate School of Engineering, Nagoya University, Furo-cho, Chikusa-ku, Nagoya 464-8603, Japan
[c] MEXT Innovative Research Center for Preventive Medical Engineering, Nagoya University, Furo-cho, Chikusa-ku, Nagoya 464-8603, Japan
[d] Baylor Institute for Immunology Research, Baylor Research Institute, 3434 Live Oak St., Dallas, TX 75204, USA
[e] Research Institute of Environmental Medicine, Stress Adaption and Protection, Nagoya University, Furo-cho, Chikusa-ku, Nagoya, 464-8601, Japan
[f] Plasma Nanotechnology Research Center, Nagoya University, Furo-cho, Chikusa-ku, Nagoya 464-8603, Japan
[g] Health Technology Research Center, National Institute of Advanced Industrial Science and Technology (AIST), Hayashi-cho 2217-14, Takamatsu 761-0395, Japan
[h] Institute for Molecular Science, National Institutes of Natural Sciences, Myodaiji Nishigo-naka 38, Okazaki 444-8585, Japan
[i] Department of Preventive Medicine, Biostatistics and Medical Decision Making, Nagoya University Graduate School of Medicine, Nagoya 466-8550, Japan

ARTICLE INFO

Article history:
Received 30 October 2009
Accepted 27 January 2010
Available online 19 February 2010

Keywords:
Semiconductor
Quantum dots (QDs)
Cell-penetrating peptides (CPPs)
In vivo imaging
Adipose tissue-derived stem cells (ASCs)

ABSTRACT

Quantum dots (QDs) have been used to study the effects of fluorescent probes for biomolecules and cell imaging. Adipose tissue-derived stem cells, which carry a relatively lower donor site morbidity, while yielding a large number of stem cells at harvest, were transduced with QDs using the octa-arginine peptide (R8) cell-penetrating peptide (CPP). The concentration ratio of QDs:R8 of 1×10^4 was optimal for delivery into ASCs. No cytotoxicity was observed in ASCs transduced with less than 16 nM of QDs655. In addition, >80% of the cells could be labeled within 1 h and the fluorescent intensity was maintained at least for 2 weeks. The ASCs transduced with QDs using R8 could be differentiated into both adipogenic and osteogenic cells, thus suggesting that the cells maintained their stem cell potency. The ASCs labeled with QDs using R8 were further transplanted subcutaneously into the backs of mice or into mice through the tail vein. The labeled ASCs could be imaged with good contrast using the Maestro *in vivo* imaging system. These data suggested that QD labeling using R8 could be utilized for the imaging of ASCs.

1. Introduction

Quantum dots (QDs) are inorganic probes that consist of CdSe/ZnS-core/shell semiconductor nanocrystals. QDs have several distinctive advantages in comparison to conventional organic labels such as a high luminance, resistance to photobleaching (long time labeling), a range of excitation wavelengths and narrower emission bandwidths [1–4]. According to these characteristics, QDs have recently been investigated as fluorescent probes for biomolecules and live cells, and are expected to be used in medical applications for diagnostics [5,6]. Various approaches have been applied to label cells with QDs, such as microinjection, electroporation, liposome-based transduction and special peptide delivery [7–11].

The transduction of QDs into cells using cell-penetrating peptides (CPPs) has been established and is thought to a useful technique because of the low cytotoxicity and high transduction efficiency. Yun Lei et al. showed that Tat peptide conjugated QDs could be transduced into mesenchymal stem cells [12]. Jui-Chih Chang et al. showed that Pep-1 labeled QDs could be transduced into stem cells and remained for about one month [13]. However, few detailed studies have so far explored the appropriate ratio of QDs and peptide, uptake time, cell function *in vitro* and application of *in vivo* imaging.

Regenerative medicine is expected to overcome the shortage of donated organs, donor site morbidity and immune reaction [14]. Many kinds of stem cells have been discovered already and provided numerous applications in regenerative medicine. Mesenchymal stem cells (MSCs) and progenitor cells are detected in various tissues, including umbilical cord blood, bone marrow, periodontal ligament and adipose tissue.

Bone marrow-derived stem cells (BMSCs) have the ability to differentiate into multiple mesenchymal cells such as cardiomyocytes, chondrocytes, osteoblasts and adipocytes.

* Corresponding author. Tel.: +81 52 719 1975; fax: +81 52 719 1977.
E-mail address: hiroshiy@med.nagoya-u.ac.jp (H. Yukawa).

0142-9612/$ - see front matter © 2010 Elsevier Ltd. All rights reserved.
doi:10.1016/j.biomaterials.2010.01.134

Therefore, BMSCs have been considered to be an important source of stem cells for use in regenerative medicine.

Recently, adipose tissue-derived stem cells (ASCs) have been increasingly recognized as multipotent stem cells and as an alternative source of BMSCs [15]. ASCs are easier to obtain in abundance by minimally invasive harvest procedures such as lipoaspiration with local anesthesia. In addition, ASCs possess the ability of self-renewing and differentiating into various mesenchymal cell types, while also secreting significant levels of many potent growth factors and cytokines, such as vascular endothelial growth factor (VEGF) and hepatocyte growth factor (HGF) [16]. Because of their potential clinical application, it has therefore become important to label the cells for tracing as transplanted cells.

Previous studies have shown that a cationic liposome (Lipofectamine) could transduce negatively charged QDs into ASCs within 4 h and the QDs remained in the cells for more than 2 weeks. However, cytotoxicity was observed at a relatively low concentration, suggesting that the major cause was the liposome (Lipofectamine) [17]. In this study, octa-arginine peptide (R8), which exhibits even greater efficiency in the delivery of several proteins, was utilized as a delivery vector and the characteristics of negatively charged carboxyl QDs transduced using R8 to live ASCs were investigated. In addition, imaging studies in subcutaneous transplantation on the back and intravenous transplantation through the tail vain were conducted.

2. Materials and methods

2.1. Animals

C57BL/6 mice were purchased from SLC Japan. The mice were housed in a controlled environment (12 h light/dark cycles at 21 °C) with free access to water and a standard chow diet before sacrifice. All conditions and handing of animals in this study were conducted with protocols approved by the Nagoya University Committee on Animal Use and Care.

2.2. Isolation and culture of ASCs

The 7–14-month-old female C57BL/6 mice were killed by cervical dislocation; adipose tissue specimens in the inguinal groove were isolated and washed extensively with Hank's balanced salt solution or phosphate-buffered saline (PBS) to remove the blood cells. The isolated adipose tissue specimens were cut finely and digested with 1 mL of 1 mg/mL typelcollagenase (Collagenase Typel, 274 U/mg, Koken Co., Ltd., Tokyo, Japan) at 37 °C in a shaking water bath for 45 min. The cells were filtrated using 250 μm nylon cell strainers (BD Biosciences) and suspended in Dulbecco's modified Eagle's medium and full-length name of F12 (DMEM/F12) containing 20% fetal bovine serum (FBS: Trace Scientific Ltd., Melbourne, Australia, Uin: 53141 Lot: B01249-500) and 100 U/ml penicillin/streptomycin (culture medium). They were centrifuged at 1200 rpm for 5 min at room temperature and adipose tissue-derived stem cells (ASCs) were obtained from the pellet. They were washed three times by suspension and centrifugation in culture medium and then were incubated overnight in culture medium at 37 °C with 5% CO_2. The primary cells were cultured for several days until they reached confluence and were defined as passage "0". The cells were used for the experiments between passages 2 and 5.

2.3. Preparation and transduction of R8-QDs complex

QDs (Invitrogen; Qdot ITK Carboxyl Quantum Dots) and R8 (Sigma genosys, Japan) were purchased. QDs were made from nanometer-scale crystals of a semiconductor material (CdSe), which are shelled with an additional semiconductor layer (ZnS) to improve their chemical and optical properties. In addition, the polymer coating has COO^- surface groups. To determine the optimal concentration ratio of QDs655 (emission at 655 nm)/R8 to transduce into ASCs, QDs655 (2.0 nM) and R8 were mixed for 20 min at room temperature in various ratios of QDs655/R8. Next, ASCs were incubated with the R8-QDs655 complex in a transduction medium (DMEM/F12, 2% FBS, 100 U/mL penicillin/streptomycin) at 37 °C. After 4 h incubation, the transduction efficiency of QDs655 into ASCs was evaluated by conventional fluorescence microscopy and a flow cytometry analysis [18].

2.4. Flow cytometry analysis

ASCs (1.5×10^5 cells) were seeded in 12-well plates (BD Biosciences) with 500 μL of culture medium for 2 h and the cells were transduced with QDs655 using R8 in transduction medium at 37 °C. After transduction, the cells were washed three times by suspension and centrifugation at 1200 rpm for 3 min. Next, the cells were suspended in 500 μL of PBS and used for flow cytometry analysis on a FACS caliber (BD Biosciences) flow cytometer using 488 nm laser excitation and 615 nm long pass emission.

2.5. Cytotoxicity of QDs to ASCs

The cells (2×10^4 cells) were seeded in 96-well plates (BD Biosciences) with 100 μL of culture medium for 2 h and then they were replaced with 100 μL of transduction medium at 37 °C. After 4 h incubation, QDs655 (0–24 nM) and R8 were mixed at the optimal ratio of 1:1 $\times 10^4$, and ASCs were transduced with QDs655 using R8 in transduction medium for 24 h. Viable cells were counted using Cell Counting Kit-8 (CCK-8; DOJINDO Laboratories Kumamoto, Japan). CCK-8 reagent (10 μL) was added to each well and the reaction was allowed to proceed for up to 4 h. The absorbance of the sample at 450 nm was measured against a background control using a microplate reader.

2.6. Proliferation of ASCs labeled with QDs

ASCs (1×10^3 cells) were seeded in 96-well plate with 100 μL of culture medium and then transduced with QDs655 using R8 at various concentrations of QDs655 for 4 h. Next, the media was replaced with 100 μL of culture medium. After 0, 2, 4 and 5 days, viable cells were counted using the Cell Counting Kit-8 in the same way.

2.7. Confocal laser scanning microscopy

A confocal laser scanning microscopy (FV1000, OLYMPUS) analysis was conducted to confirm the fluorescent intensity and location of QDs655 in labeled ASCs using R8. Images obtained from the bottom of the coverslip to the top of the cells were recorded and each image was superimposed on PC to qualify the total brightness and pixel area of each region of interest. Before imaging, the cells were washed three times with PBS and replaced with fresh transduction medium [19].

2.8. Transduction of QDs using R8

ASCs were preincubated in the transduction medium with 10 mM sodium azide and 2-deoxy-D-glucose (endocytosis inhibitors) for 1 h at 37 °C, or 3 mM amiloride (macropinocytosis inhibitor) for 10 min at 37 °C. In addition, ASCs were preincubated in the transduction medium for 30 min at 4 °C (both endocytosis and macropinocytosis inhibitors). These cells were then washed three times with PBS followed by the addition of 0.4 nM QDs655 with R8 in fresh transduction medium for 1 h. Thereafter, the cells were observed using confocal laser scanning microscopy.

2.9. Adipogenic differentiation

Adipogenic differentiation was induced by culturing the cells for 3 days in DMEM (high glucose) containing 100 μM indometacin, 1 μM dexamethasone, 1 μM hydrocortisone, 10 μM insulin (Sigma, I-5500) and 10% FBS. The cells were then further cultured in DMEM (high glucose) containing 10% FBS for 2 weeks and the medium was changed every 3 days. Differentiation was confirmed by conventional microscopic observations of intracellular lipid droplets and Oil Red O staining as an indicator of intracellular lipid accumulation. Briefly, the cells were fixed in 10% solution of formaldehyde in PBS for at least 10 min at room temperature and then were washed with 60% isopropanol. Next, the cells were stained with 2% (w/v) Oil Red O reagent for 10 min at room temperature followed by repeated washing with distilled water and destaining in 100% isopropanol for 1 min.

2.10. Osteogenic differentiation

Osteogenic differentiation was induced by culturing the cells for 2 weeks in DMEM containing 200 μM dexamethasone, 50 μM ascorbate-2-phosphate (Wako Pure Chemical Industries Ltd., 013-12061), 10 mM α-glycerophosphate (Sigma, G-9891) and 10% FBS. The differentiation was confirmed by staining for any alkaline phosphatase activity and then observing the extracellular matrix calcification using Von Kossa's method. The cells were washed twice with PBS and fixed in 10% formalin for 15 min at room temperature. They were washed and incubated with deionized water for 15 min. Then, they were stained with a solution containing naphtol AS MX-PO_4 (Sigma, N-5000), *N,N*-dimethylformamide (Wako Pure Chemical Industries Ltd.), Red Violet LB salt (Sigma, F-1625) and Tris–HCl buffer (pH 8.3) for 45 min. Von Kossa staining was carried out with 2.5% silver nitrate solution for 30 min.

2.11. RNA extraction and real-time RT-PCR

Total RNA was extracted from cells by using RNeasy® reagent (QIAGEN) according to the manufacturer's instructions. cDNA synthesis and amplification via PCR were performed using Transcriptor High Fidelity cDNA Synthesis Kit (Roche Diagnostics GmbH, Mannheim, Germany). The cDNA was used for PCR by LightCycler® FastStart DNA Master PLUS SYBR Green I (Roche). The PCR reaction mixture was made up in 20 μL of 10 μM targeted gene oligonucleotides primers. Using LightCycler® (Roche), heat denaturation at 95 °C for 10 min and 40 cycles of PCR

Table 1
Primer sequences used for real-time RT-PCR.

Gene	Accession	Sense primer	Antisense primer
ALP	NM_007431	GTTGCCAAGCTGGGAGAACAC	CCCACCCCGCTATTCCAAAC
β-Actin	NM_007393	TATGGAATCCTGTGGCATCC	CTTCTGCATCCTGTCAGCAA

with denaturing at 95 °C for 10 s, annealing temperature 55 °C for 10 s and extension at 72 °C for 10 s were performed ALP and β-Actin. The sequences of all primers are shown in detail in Table 1.

2.12. In vivo fluorescent imaging of ASCs labeled with QDs

QDs655, QDs755 or QDs800 were transduced into ASCs using R8 in the same way. ASCs (0.5, 1 and 3 × 10^5 cells) labeled with QDs were subcutaneously transplanted with 50 μL PBS into the back of C57BL/6 mice. Images were taken using the Maestro *in vivo* imaging system (CRI Inc, Woburn, MA; excitation filter: 575–605 nm, emission filter: 645 nm long pass). The detection was set to capture images automatically at 10-nm increments from 630 nm to 850 nm with constant 1 s exposure. The resulting TIFF images were loaded into the vendor's software and analyzed.

On the other hand, for the *in vivo* imaging of ASCs transplanted into mouse through the tail vain, ASCs (5 × 10^5 cells) labeled with QDs800 were injected with 0.15 mL saline. Images were taken using the Maestro *in vivo* imaging system in the same way after 10 min. Moreover, for the histological analysis, ASCs (5 × 10^5 cells) labeled with QDs655 were injected into the mouse. The mouse was then sacrificed after 10 min and major organs (heart, lung, liver, spleen and kidney) were harvested and washed three times with PBS to remove retained erythrocytes. The collected tissue specimens were then fixed by formalin and embedded in paraffin. To examine the histological QDs uptake and distribution of transplanted ASCs, the tissue specimens were cut into 10 μm thick sections and then were observed by fluorescent microscopy.

2.13. Statistical analysis

Numerical values are presented as the mean ± SD. Each experiment was repeated three times. Statistical significance was evaluated using unpaired Student's *t*-test for comparisons between the two groups; *p*-values < 0.05 were considered to be statistically significant. All statistical analyses were performed using the SPSS software package.

3. Results

3.1. Transduction of QDs into ASCs using R8

QDs655 (2.0 nM) were mixed with concentrations of R8 (0, 0.2, 2.0, 20 and 200 μM) for 20 min respectively and they were tested for their ability to transduce into ASCs using conventional fluorescent microscopy and flow cytometry analysis. Red fluorescence derived from QDs655 was strongly observed at the ratio of 20 μM R8 to 2.0 nM QDs655. Increasing the R8 peptide concentration beyond 20 μM did not increase the QDs655 internalization. This result suggests that the concentration ratio of QDs:R8 of 1:1 × 10^4 is optimal for delivery into ASCs (Fig. 1A).

3.2. Cytotoxicity to ASCs

QDs655 was transduced into ASCs using R8 at various concentrations in transduction medium for 24 h at 37 °C. Significant cytotoxicity was observed in ASCs transduced with more than

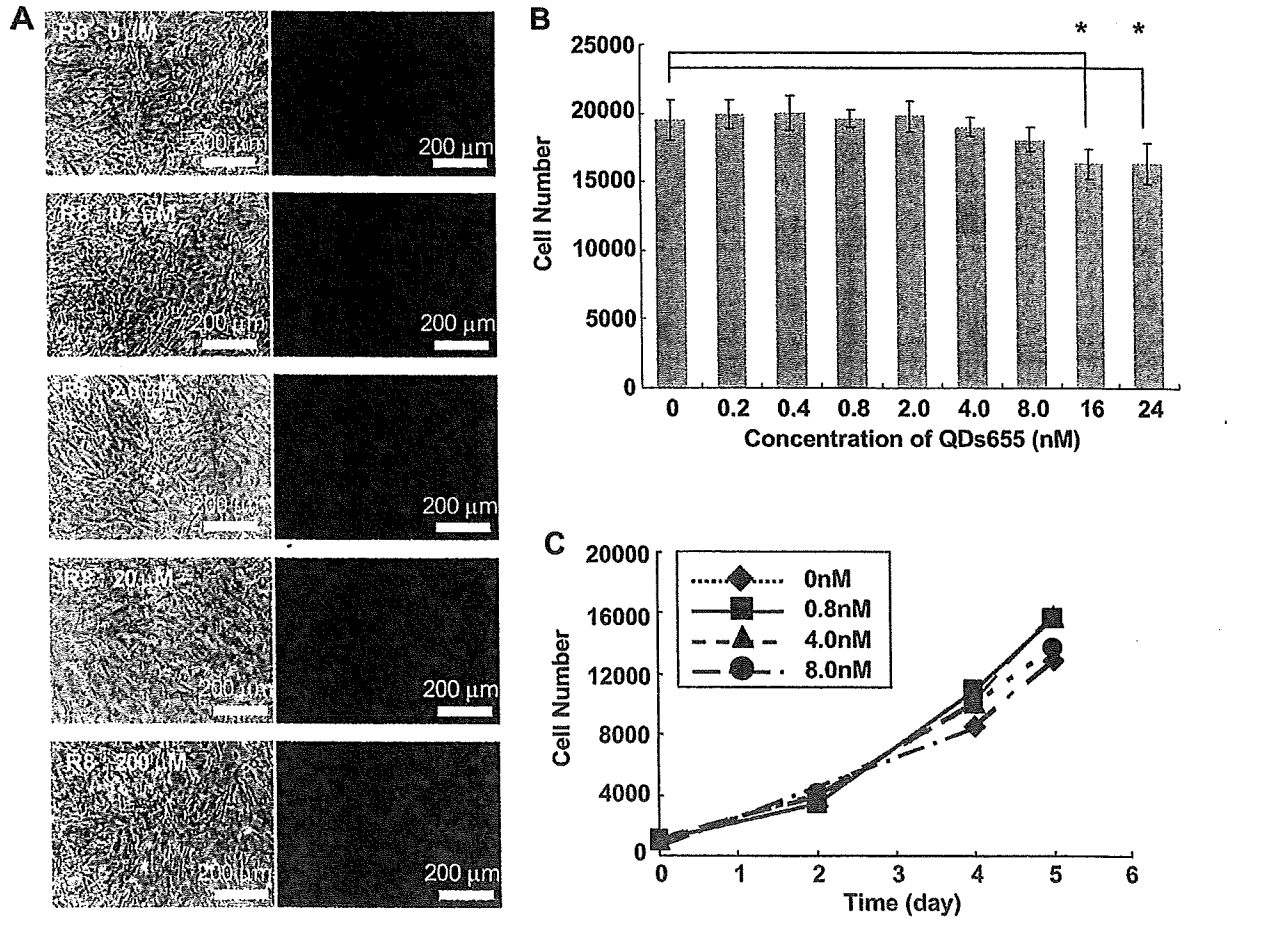

Fig. 1. Optimal formation of R8-QDs and the cytotoxicity to ASCs. A: QDs655 (2.0 nM) were mixed with various concentrations of R8 for 20 min and the complex were transduced into ASCs for 4 h to determine the optimal concentration ratio of QDs/R8. B: ASCs were transduced with QDs655 using R8 at various concentrations for 24 h. The survival of ASCs transduced with QDs655 using R8 is compared with non-transduction ASCs. C: The proliferation rate is shown in the nontoxic range of QDs655. The number of cells was estimated at 0, 2, 4, and 5 days after transduction as described in Materials and Methods. The data, all in triplicate, are shown as the mean ± SD values. *$p < 0.05$.

16 nM of QDs655, however, >80% of the cells were still alive. In addition, no remarkable cytotoxicity was observed with less than 8.0 nM of QDs655 (Fig. 1B). The morphology and fluorescent images were confirmed by conventional fluorescent microscopy.

Moreover, the influence on the proliferation rate was examined within the non-cytotoxic range of concentrations. The cells were confirmed to exhibit a logarithmic growth rate that was nearly equal to normal ASCs. There were no significant differences in these concentrations (Fig. 1C). These data suggest that ASCs could be labeled within an 8.0 nM concentration of QDs using R8.

3.3. Transduction efficiency of QDs using R8

To determine the transduction efficiency of QDs into ASCs, ASCs were transduced with QDs655 using R8 for 1 h at 0, 0.8, 2.0 and 8.0 nM concentrations of QDs655. The internalization of QDs655 was estimated and compared using flow cytometry analysis. The transduction efficiency of QDs655 after 1 h transduction was 81.4 ± 5.4% at 0.8 nM, 90.8 ± 2.8% at 2.0 nM and 95.2 ± 1.9% at 8.0 nM (Fig. 2A). More than 80% of the cells could be labeled within 1 h (Fig. 2B).

In addition, the location and fluorescent intensity of QDs655 was analyzed using confocal laser scanning microscopy at a concentration of 0.4 nM QDs655 after 1 h of transduction. The successive location of QDs655 in the ASCs was observed in 1 h, 8 h, 1 day, 7 days, 10 days and 14 days after transduction. QDs655 were widely dispersed in the cell cytoplasm during the early time points, however, aggregation of QDs655 was observed as time passed, QDs655 could not be observed in the nuclei at any time (Fig. 3A). The fluorescent intensity level of QDs655 was approximately equal during 14 days (Fig. 3B).

3.4. Transduction of QDs using R8 by macropinocytosis

The internalization of QDs655 using R8 with sodium azide and 2-deoxy-D-glucose, or amiloride, or at 4 °C was compared to that of normal transduction. The fluorescence of QDs655 could be observed on the face of the ASCs only and not in the cytoplasm (Fig. 4A–C). On the other hand, QDs655 were incorporated into the cytoplasm of ASCs after no application of inhibitors (Fig. 4D). These results suggested that the internalization of QDs655 using R8 occurs mainly by macropinocytosis.

3.5. Differentiation of ASCs transduced with QDs using R8

To examine the influence on the pluripotency of ASCs, ASCs were transduced with 0.4 nM of QDs655 using R8 and cultured with adipogenic and osteogenic medium for 2 weeks. Following adipogenic differentiation, intracellular lipid droplets in ASCs labeled with QDs655 were observed in the same frequency as the control ASCs and the red fluorescence derived from internalized QDs655 was confirmed (Fig. 5A-a). Oil Red O staining confirmed that intracellular droplets were lipid (data not shown). On the other hand, after incubation in osteogenic medium, ASCs labeled with QDs655 became osteocyte-like in morphology with cuboidal shapes (Fig. 5A-b). The cells were positive for von Kossa's staining in the same frequency as the control ASCs (data not shown). Red fluorescence of QDs655 was clearly observed for more than 2 weeks using confocal laser scanning microscopy in both of the differentiated cell types. However, the fluorescence of QDs655 was only slightly observed in the ASCs cultured with normal culture medium (Fig. 5A-c).

Moreover, to estimate the influence on osteogenic differentiation ability of ASCs at the mRNA revel, ALP activity was measured by real-time RT-PCR. ALP activity of ASCs transduced with QDs655

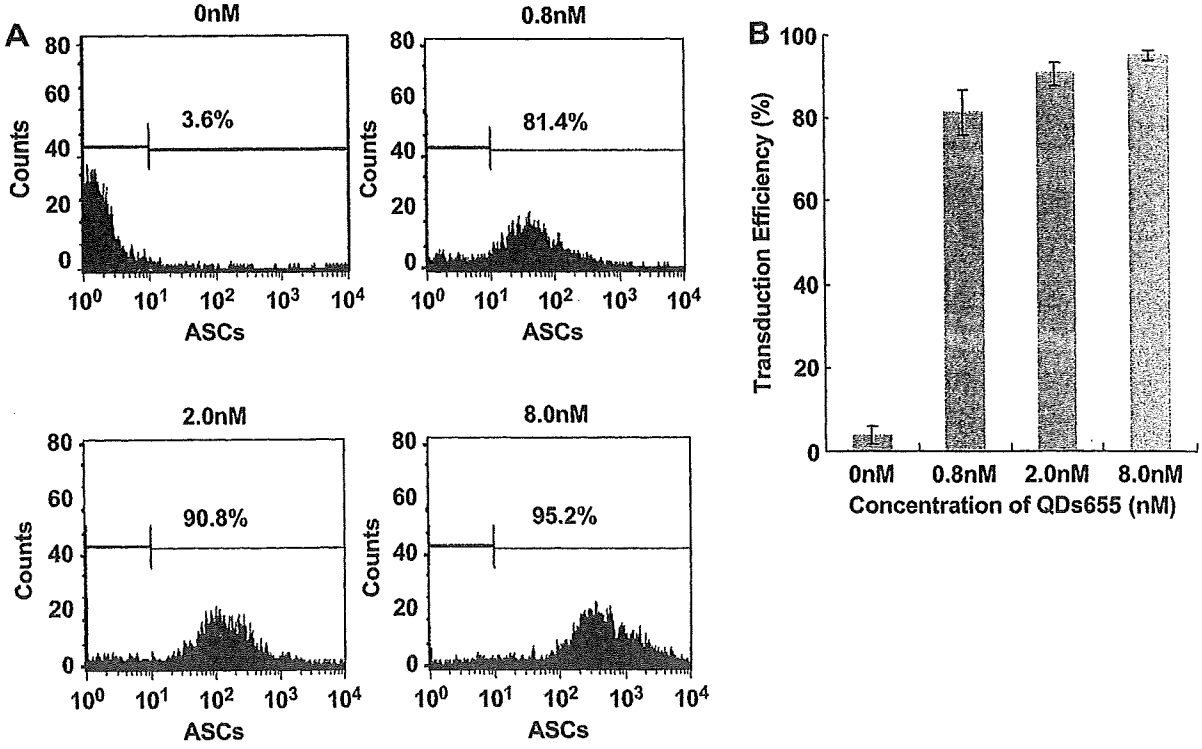

Fig. 2. Transduction efficiency of QDs using R8 quantified by flow cytometry. A: The transduction efficiency of QDs655 into ASCs using R8 after 1 h of incubation was quantified by flow cytometry. The mean fluorescent units are the average of 10,000 units. B: The bar graph shows the transduction efficiency of QDs655 using R8 after 1 h of transduction.

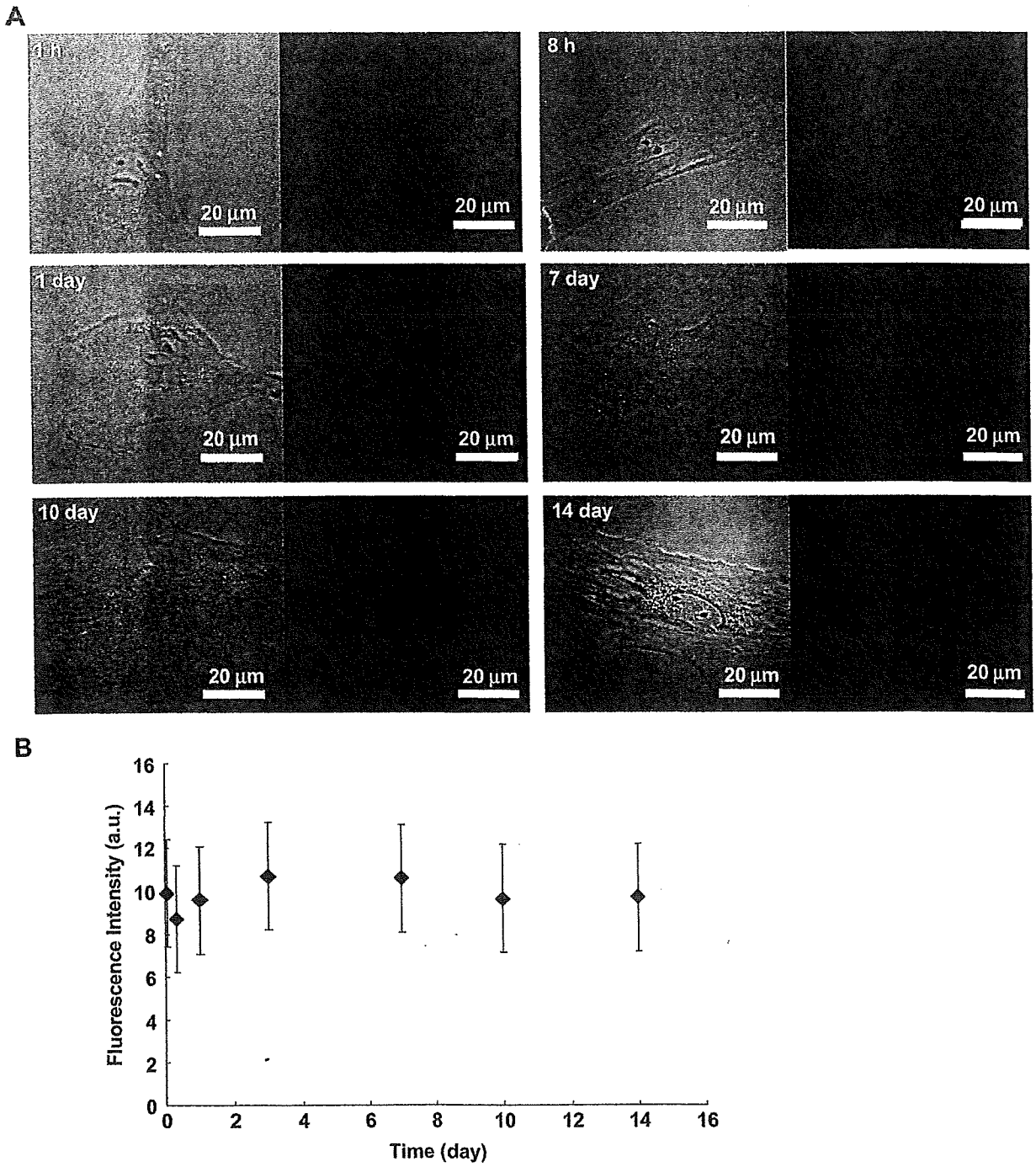

Fig. 3. Intracellular distribution and fluorescence intensity of QDs. A: The intracellular distribution of QDs655 in 1 h, 8 h, 1 day, 7 days, 10 days and 14 days after transduction were obtained by confocal laser scanning microscopy. Internalized QDs655 are shown by the red fluorescence. B: The fluorescence intensity was measured by confocal laser scanning microscopy. The data, in each triplicate, are shown as the mean ± SD values.

using R8 in osteogenic differentiation was observed at the same level as that of the non-transduced ASCs (Fig. 5B and C). These data suggested that the differentiation ability of ASCs was not inhibited by QDs655 transduction using R8.

3.6. Detection sensitivity for in vivo imaging

ASCs (0.5×10^5, 1.0×10^5 and 3.0×10^5 cells) labeled with QDs655 using R8 were injected subcutaneously with saline into the back of the mice. The Maestro Optical Imaging System (excitation filter: 575–605 nm, emission filter: 645 nm long pass) was used to observe the mice 1 h after transplantation. Moreover, images were obtained 1, 2, 5 and 7 days after transplantation (Fig. 6A) and the intensity was evaluated (Fig. 6B). The results suggested that ASCs labeled with QDs655 could be detected up to 7 days following subcutaneous transplantation.

On the other hand, one of the advantages of QDs is their ability for multiplex imaging. Multiplex imaging may be applied for

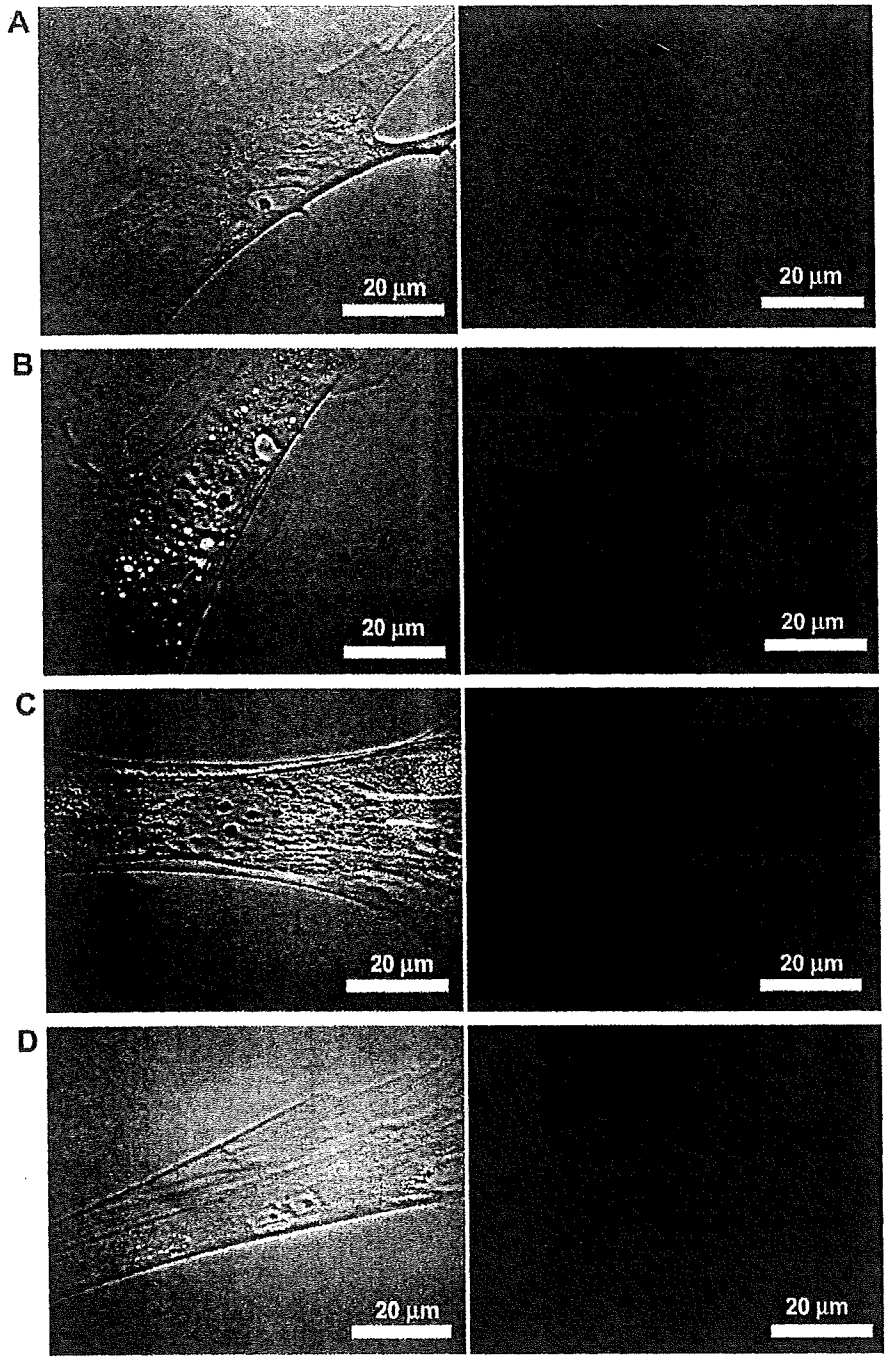

Fig. 4. Transduction mechanism of QDs using R8 into ASCs. A: ASCs were preincubated in the transduction medium with 10 mM sodium azide and 2-deoxy-D-glucose (endocytosis inhibitors) for 1 h at 37 °C. B: ASCs were preincubated in the transduction medium with 3 mM amiloride (macropinocytosis inhibitor) for 10 min at 37 °C. C: ASCs were preincubated in the transduction medium for 30 min at 4 °C (both endocytosis and macropinocytosis inhibitors). These cells were washed three times with PBS followed by addition of 0.4 nM QDs655 using R8 in the fresh transduction medium for 1 h. D: ASCs were incubated with 0.4 nM QDs655 with R8 under the normal transduction condition. These cells were observed using confocal laser scanning microscopy.

tracing different cell populations at the same time. Almost all kinds of QDs can be excited by the same wavelength and a different wavelength of light is emitted depending on the size of the QDs. In this study, ASCs (1×10^5 cells) were labeled with QDs655, 705 and 800 using R8 respectively and subcutaneously transplanted into the back of the mice and the multiplex image in 1 h was obtained in 1 h after transplantation (Fig. 6C).

Furthermore, ASCs labeled with QDs800 using R8 were transplanted through the tail vein of a mouse to examine whether the fluorescence of QDs800 from the ASCs could be detected and demonstrate the distribution of transplanted ASCs. When the mouse was sacrifice after 10 min, the fluorescence of QDs800 could be detected in the lung only by the Maestro *in vivo* imaging system (Fig. 7A). On the other hand, a histological analysis showed that the

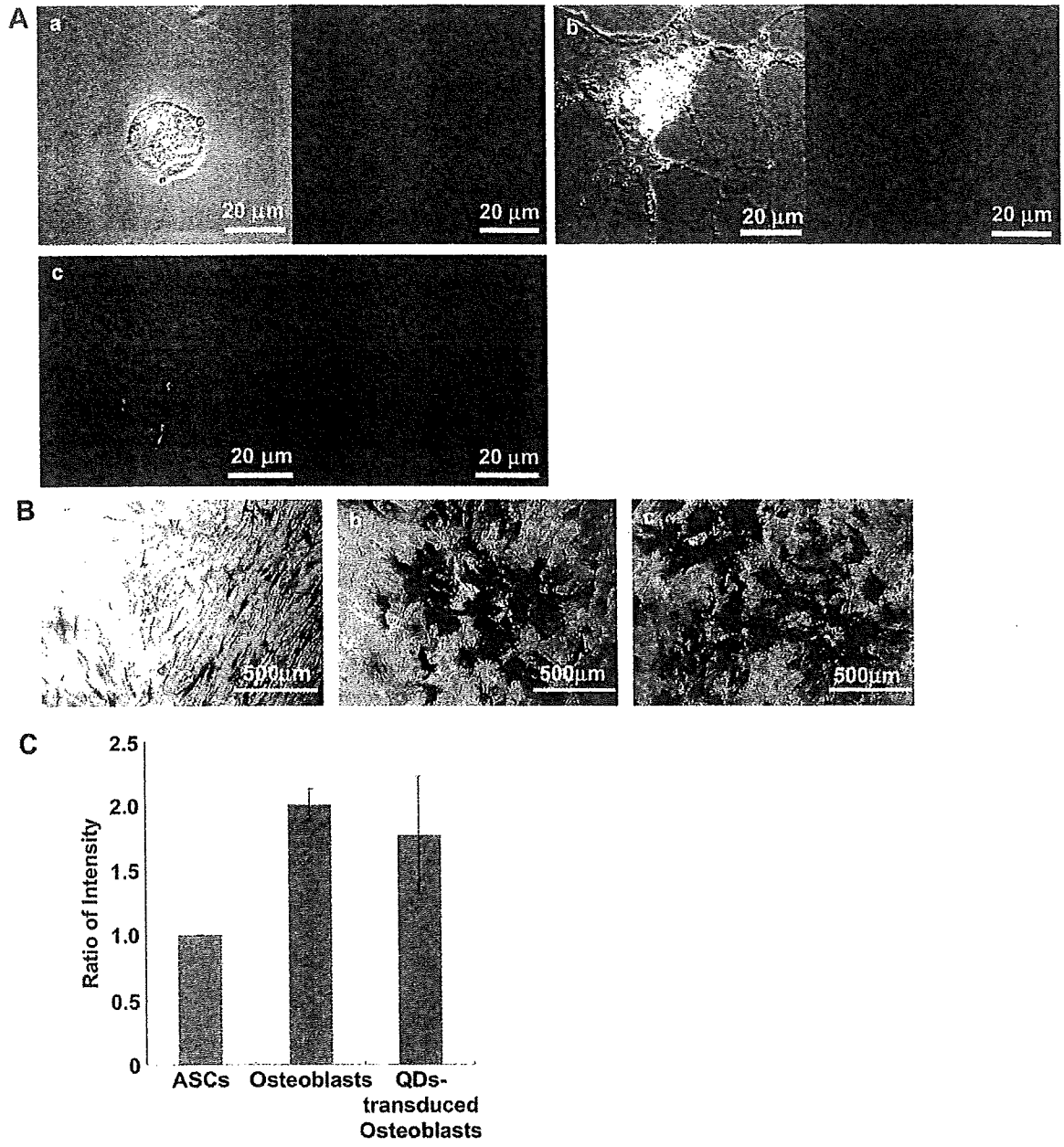

Fig. 5. Differentiation of ASCs transduced with QDs using R8. A: ASCs transduced with QDs655 (0.4 nM) using R8 were differentiated to lipocytes (a) or osteocytes (b) for 2 weeks. ASCs transduced with QDs655 (0.4 nM) using R8 were incubated in the culture medium without differentiation (c). These figures were obtained using confocal laser scanning microscopy. Phase contrast (left) and QDs655 fluorescent (right) were shown. B: Negative ALP staining of normal cultured (non-differentiated) ASCs (a), positive ALP staining of osteogenic induced ASCs (b) and osteogenic induced ASCs transduced with QDs655 using R8 (c) were confirmed. C: The quantification of ALP mRNA levels was compared in three groups. There was no significant difference between non-transduced ASCs and ASCs transduced with QDs655 using R8 ($p > 0.05$), but significantly more ALP activity was expressed than in the control ASCs ($p < 0.05$).

presence of ASCs could be confirmed in slices of the lungs only using conventional fluorescent microscopy (Fig. 7C). The heart and kidney data were not shown.

4. Discussion

Several studies have reported that some cells could passively internalize QDs in the culture medium without carrier or microinjection, electroporation and liposome-based transduction [7,11]. ASCs could not be transduced with QDs only without the help of carriers (data not shown). A cationic liposome "Lipofectamine" was used for the transduction of QDs into ASCs without further modification [17]. However, cytotoxicity was observed at a comparatively low concentration of >2.0 nM. In addition, the transduction time was relatively long (4 h at 0.8 nM of QDs655). Recently, CPPs mediated transduction has attracted more and more attention for the efficient cellular membrane delivery and labeling [12,20,21].

R8 which exhibits even greater efficiency in the delivery of several proteins was employed in order to overcome these problems. Moreover, compared with other articles [4,7,8], the transduction efficiency of R8 seems to be similar to CLO-Tat, CHPNH2 and pep-1. On the other hand, the molecular length of R8 is shorter